Crustal structure and geodynamics of the eastern Qilian orogenic belt, NE margin of the Qinghai-Tibet plateau, revealed by teleseismic receiver function

Yongzhi Cheng[1,2], Rui Gao[1,2,3]*, Jiuhui Chen[4], Zhanwu Lu[1,2]*, Wenhui Li[1,2], Guangwen Wang[1,2], Hao Chen[5], Rubing Han[6], Xiao Niu[7], Guowei Wu[1,2], Si Chen[1,2] and Yuguo Cai[1,2]

[1]Institute of Geology, Chinese Academy of Geological Sciences, Beijing, China, [2]SinoProbe Laboratory of Ministry of Natural Resources, Beijing, China, [3]School of Earth Sciences and Engineering, Sun Yat-sen University, Zhuhai Campus, Zhuhai, Guangdong, China, [4]State Key Laboratory of Earthquake Dynamics, Institute of Geology, China Earthquake Administration, Beijing, China, [5]School of Geophysics and Measurement-Control Technology, East China University of Technology, Nanchang, Jiangxi, China, [6]Department of Mathematical Sciences, Tsinghua University, Beijing, China, [7]SinoProbe Center-China Deep Exploration Center, Chinese Academy of Geological Sciences, Beijing, China

The eastern segment of the Qilian orogenic belt, comprising the Linxia block and Longzhong block, is at the Qinghai−Tibet Plateau's northeastern margin. The area has experienced multiple tectonic events, including closure of the Qilian Ocean, convergence of the North China block and Qilian terrane, and collision of the Indian and Eurasian plates, forming a complex tectonic framework. To investigate the area's geological evolution and the suture's current location between the blocks, we used 3-year data recorded by 33 portable ChinArray II broadband stations (2013−2016). Using three teleseismic P-wave receiver function methods, H-κ stacking and common conversion point stacking (CCP), crustal structure, Poisson's ratio, and Moho morphology were obtained at 33 stations. The results are described as follows: 1) The Maxianshan fault is an important boundary fault that divides the Linxia block and Longzhong block. The Linxia block's layered crustal structure is obvious, and there is a low-velocity anomaly in the middle and lower crust, which may contain saline fluid and has Japanese-type island arc characteristics. 2) The layered structure of the Longzhong block's upper crust is significant, while the middle and lower crust's layered structure is weak with weak low-velocity characteristics and oceanic-island basaltic crust characteristics. The Longzhong block may have originally been formed by Mariana-type island arcs. 3) The Conrad interface and Moho lateral variation in the Ordos block's southwestern margin are weak, showing stable craton characteristics. 4) Our results show that the Maxianshan fault cuts through the Earth's crust and is a continuous west-dipping negative seismic phase in the Common Conversion Point section. The fault zone is the suture line between the Linxia block and Longzhong block. 5) The middle and upper crust of the Liupanshan tectonic belt is thrust upwards on the Ordos block's southwestern margin, providing deep structural evidence of the Cenozoic uplift of the Liupanshan structural belt.

Introduction

With the demise of the Neo-Tethys Ocean at ~50 Ma, the Indian plate and the Eurasian plate experienced continent–continent collision (e.g., Tapponnier et al., 2001; Yin and Harrison, 2000). The continuous northwards subduction of the Indian plate created the Qinghai–Tibet Plateau, the largest and highest plateau in the world. As a natural laboratory to study continent–continent collision and plateau uplift, the Qinghai–Tibet Plateau has attracted much research focus. With a thick lithospheric crust that is twice the global average crustal thickness (Zhong and Ding, 1996; Ji et al., 2009), how did the Qinghai–Tibet Plateau grow and evolve? Geologists and geophysicists have proposed many plateau growth and expansion models based on different research methods and results (Clark and Royden, 2000; Tapponnier et al., 2001; Wu et al., 2022; Shi et al., 2022; Gao et al., 2022; Ding et al., 2022). Due to different research methods, limited data for establishing evolutionary models, and the structural complexity of the Qinghai–Tibet Plateau, there is no unified understanding of the plateau's uplift and expansion mechanism. From the Qinghai–Tibet Plateau's formation to the present, the evolution of its lithospheric crust has experienced much horizontal shortening and obvious vertical thickening (Wang et al., 2017; Xu et al., 2018; Gao et al., 2022). Under the double action of lateral extrusion and vertical gravity load, the plateau is still expanding, resulting in obvious intracontinental deformation and tectonic activity in surrounding areas. Examples include crustal shortening, regional tectonic activation, intracontinental orogeny, and frequent earthquakes (Tong et al., 2007; Hao et al., 2021; Wei et al., 2022). Since the deep matter of the Qinghai–Tibet Plateau is still expanding to the periphery, the Haiyuan–Liupanshan tectonic belt is restricted by the Alxa block and the Ordos block. Crust and mantle materials with different properties converge here, leading to frequent earthquake disasters and strong tectonic activity in front of the Qinghai–Tibet Plateau's northeastern margin (Chen et al., 2005; Liu et al., 2006). The eastern segment of the Qilian orogenic belt is composed of the Linxia block and the Longzhong block, and it is now represented by the basin's geomorphic features. It is at the forefront of the Qinghai–Tibet Plateau's northeastern margin, comprising a "rhombic-shaped area" controlled by multiple large, deep boundary faults, where the Qilian–Qaidam, western Qinling, Alxa, and Ordos blocks meet (Song et al., 2006; Figures 1A, B). The Haiyuan Fault and Tianjingshan Fault jointly control the contact relationship between the Alxa block and Longzhong block. The eastern part of the Longzhong block is connected to the southwest edge of the Ordos block by the Liupanshan fault zone. The electrical structures on both sides of the Maxianshan fault zone are significantly different, where a pillow-shaped basaltic rock belt is exposed (Pei et al., 2006; Song et al., 2006), forming the boundary between the Linxia block and the Longzhong block (Xin et al., 2021; Figures 1A, B). Since the Cenozoic loess strata in the Linxia block and the Longzhong block are heavily covered and the deep bedrock is rarely exposed, research on the suture line position and the structural boundary of the Linxia block and Longzhong block is scarce. The Liupanshan structural belt is the front edge of the Qinghai–Tibet Plateau's northeastern margin (Zhang et al., 2004) and is part of the transition zone between the arc-shaped structural belt on the northeastern margin and the Ordos block.

Simultaneously, it is also the confluence zone of the central orogenic belt. This unique tectonic system has become the focus area for studying the east–west and north–south tectonic transformations of the Chinese mainland (Zhang et al., 2004). The deep structure and uplift history of the Linxia block, Longzhong block, and Liupanshan structural belt are closely related to the tectonic evolution of the Qinghai–Tibet Plateau. Therefore, studying the deep structure of the Linxia block, Longzhong block, and Liupanshan tectonic belt and their territories is key to understanding the plateau's growth and evolution and intracontinental deformation.

Geological setting

The eastern section of the Qilian orogenic belt on the Qinghai–Tibet Plateau's northeastern margin is composed of the Linxia block and Longzhong block, with the Maxianshan fault as the dividing line between them (Guo et al., 2016; Xin et al., 2021). The eastern side of the study area crosses the Liupanshan tectonic belt and enters the southwest margin of the Ordos block, and its northern side is bounded by the Haiyuan fault and Xiangshan–Tianjingshan fault, which extends to the Alxa block. Our study area is at the forefront of the Qinghai–Tibet Plateau's northeastern margin, comprising a "rhombic-shaped area" controlled by multiple large, deep boundary faults, where the Qilian–Qaidam, western Qinling, Alxa, and Ordos blocks meet (Song et al., 2006; Figures 1A, B). Geomorphologically, this area is on the boundary line between the Qinghai–Tibet Plateau's northeastern plateau and the North China hills. This boundary line is a zone of first-level landform change and the main structural junction of the east–west and north–south differentiation of the Chinese mainland (Zhan et al., 2017). The research area is jointly controlled by many deep faults, including the Tianjingshan Fault and Haiyuan–Liupanshan Fault, and the above faults with thrust–nappe and strike-slip characteristics have created a series of NW–SE-trending mountains (Tapponnier et al., 2001; Cheng et al., 2022). Tectonically, the area is at the intersection of the South–North seismic zone and the Central China Orogenic Belt (Yin and Zhang, 1998). The Qinghai–Tibet Plateau, Ordos block, and Alxa block constitute a quasitriple junction structure, which is an ideal place to study collisional orogeny and the interaction mechanism between blocks (Tian and Ding, 1998; Li et al., 2006; Cheng et al., 2019; 2022). The area has a very high earthquake density, and two of the 23 seismic belts in China (Liupanshan belt and Lanzhou–Tianshui belt) are located here. Historically, the Haiyuan magnitude 8.5 earthquake, Gulang magnitude 8.0 earthquake, and Changma magnitude 7.6 earthquake occurred in 1920, 1927 and 1932 in this area, respectively. Therefore, the research area is a natural laboratory for studying the plateau's growth and evolution.

Predecessors have conducted much geophysical work on the northeastern margin of the Qinghai–Tibet Plateau. Surface GPS observations show that this area has experienced strong compressive tectonic stress from the Qinghai–Tibet Plateau to its northeastern edge, and the direction of compressive stress gradually transitions from northeast to nearly east–west and nearly southeast (Zhang et al., 2004; Gan et al., 2007). Predecessors have done research on P-wave receiver function, S-wave receiver function, rayleigh-wave Eikonal tomography, joint inversion of receiver functions and rayleigh wave dispersions, joint inversion of receiver functions
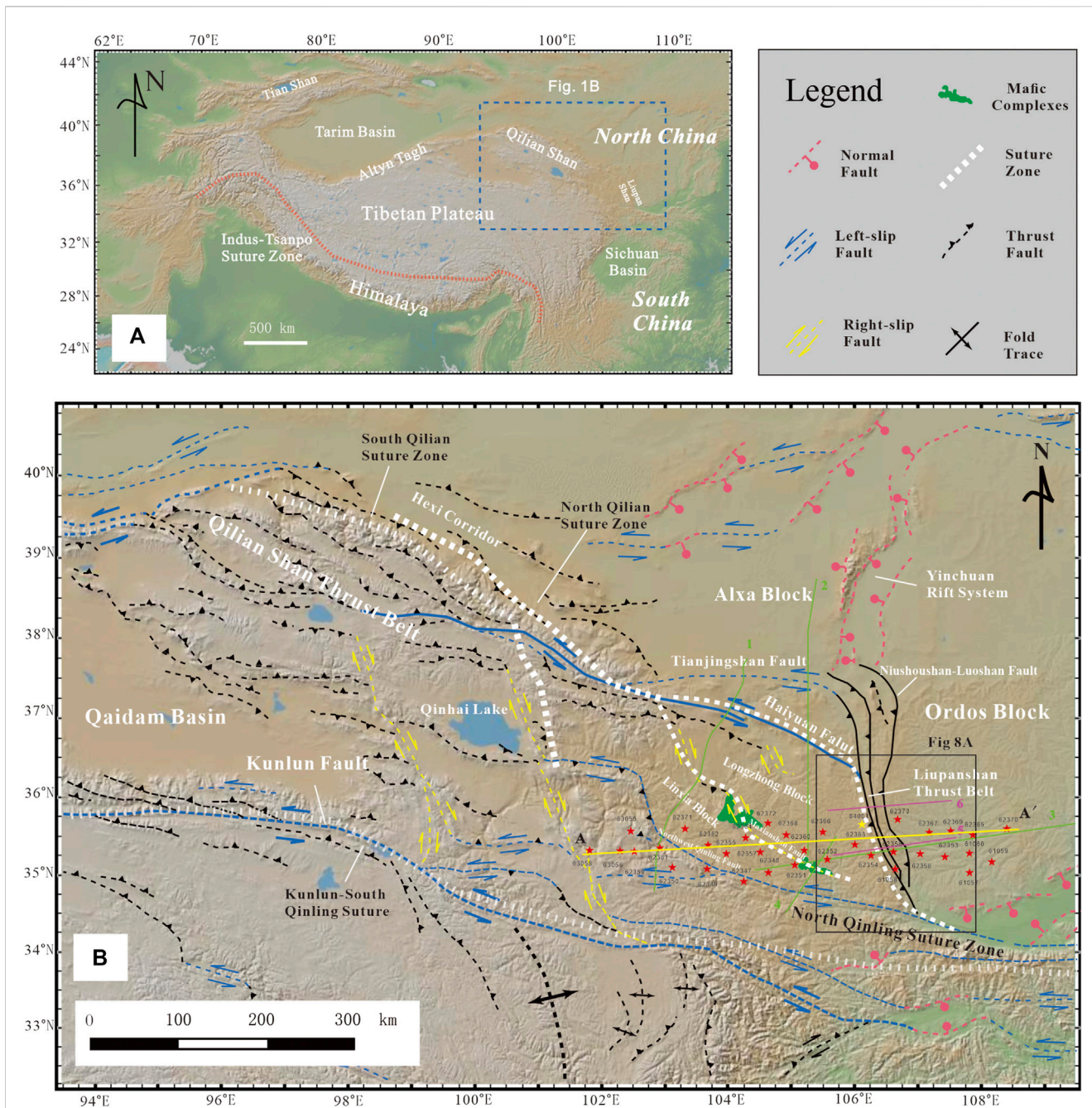
FIGURE 1
(A) Digital topographic map of the Himalayas, Tibet, and the surrounding region from GeoMapApp.org. Additionally, the location of part B and the main regional tectonic features are shown. **(B)** Structural overview of the Qinghai–Tibet Plateau's northeastern margin and its adjacent areas (image from GeoMapApp.org). The structures shown in the map follow those of Burchfiel et al. (1989); Gaudemer et al. (1995); Taylor and Yin (2009). The red pentagon represents the station location. The yellow solid line (AA) is the position of the CCP stacking section, and green lines 1–4 represent the magnetotelluric profile (1. Jin et al., 2012; 2. Xia et al., 2019; 3. Han et al., 2016; 4. Xin et al., 2021). Purple lines 5–6 represent the seismic detection profile (5. Guo et al., 2016; 6; Tian et al., 2021).

and Bouguer gravity anomaly by using ChinArray II broadband stations data (Wang et al., 2017; Xu et al., 2018; Hao et al., 2021; Shi et al., 2022; Wei et al., 2022; Wu et al., 2022). The detection of artificial source earthquakes and natural earthquakes shows that, compared with the Ordos block in the northeast and the Alashan block in the north, the crust of the northeastern margin of the Qinghai–Tibet Plateau has significantly thickened (Li et al., 2006;

Liu et al., 2006; Gao et al., 2013; Tian and Zhang, 2013; Gao et al., 2022). The crustal thickness of the West Qinling orogenic belt and the Longxi Basin is 54–48 km (Liu et al., 1996; Chen et al., 2005; Zhang et al., 2013), the Qaidam Basin is 50–53 km (Teng, 1974; Zeng et al., 1994; Cui et al., 1995), and the Qilian Mountains and Kunlun fault zone are 60–70 km (Vergne et al., 2002; Li et al., 2004; Karplus et al., 2011; Zhang et al., 2011). However, large differences remain

among different scholars on the scientific issues of the mechanism and crustal thickening method; ambient noise tomography has revealed that there is a large-scale low-velocity anomaly 30–50 km below the Qinghai–Tibet Plateau's northeastern margin, which is believed to be caused by lower crustal flow activities (Zheng et al., 2010), although artificial source seismic detection studies have found that the lower crust of the Qinghai–Tibet Plateau's northeastern margin thickened (Liu et al., 1996; Liu et al., 2006; Jia et al., 2009; Zhang et al., 2011; Wang Q. et al., 2013). However, comparing the structure of the seismic wave velocity and Poisson's ratio, some scholars believe that the crust of the northeast margin is acidic, the felsic content is high, and its density is lower than that of ferromafic components, thus reducing the seismic wave velocity and Poisson's ratio of the middle–lower crust; the northeast margin's lower crust is likely a crustal layer lacking ferromafic minerals (Liu et al., 2008a). Some scholars also believe that the lower crustal Poisson's ratio occurs because the scale of the felsic upper crust is thicker than that of the mafic lower crust (Galvé et al., 2002; Li et al., 2006; Tian and Zhang, 2013). The results of three-dimensional lithospheric S wave velocity model show multiple processes contributed to the crustal deformation in NE Tibet and Western Alxa block and southwestern Ordos block have been modified (Wang et al., 2017). Multi-station receiver-function gathering imaging results show that the deformation of the NE Tibet is accomplished by whole lithospheric shortening (Xu et al., 2018). Crustal flow develops in the lower crust of the northeastern Tibetan Plateau is revealed by Rayleigh wave Eikonal Tomography, but the crustal flow is resisted by surrounding blocks, resulting in pure shear deformation (Hao et al., 2021). Shi et al. (2022) obtained the crustal thicknesses and average Vp/Vs ratios via joint estimation from teleseismic P-wave receiver functions and the complete Bouguer gravity anomaly, the results support the previous hypothesis of upper-crust thickening or lower-crust delamination of the coherent thickening crust. The S receiver function results show thin mantle lithosphere in the Qilian and West Qinling Orogens and thick one beneath the Longxi Basin (Wei et al., 2022). Additionally, Zhang et al. (2013) found a set of seismic wave low-velocity layers that deepen southwards in the upper crust from the southern margin of Alxa to the bottom of the middle Qilian block and proposed that this low-velocity layer may have played a key role in the crustal deformation of the plateau's northeastern margin.

In summary, although many geological and geophysical exploration studies have been conducted on the Qinghai–Tibet Plateau's northeastern margin, most of the research results are presented in two-dimensional sections, and different scholars have different concerns. The existing research is insufficient to establish a crustal deformation model recognized by most scholars. Thus, it is necessary to first clarify the contact relationships between different blocks on the Qinghai–Tibet Plateau's northeastern margin and its deep crust–mantle structure. Therefore, this study uses ChinArray II broadband seismic data, through manual data selection, and the extraction results of P-wave receiver functions (PRFs) to study the crust–mantle structure of the Linxia block, Longzhong block, and Liupanshan tectonic belt. Based on our results and combined with previous geochemical and petrological results, we established the

tectonic evolution of this area and determined the location of the suture formed by the intersection of the Qaidam–Qilian block and North China block. The deep structure, contact relationship, and resource effect of the Linxia block, Longzhong block, and Ordos block are discussed.

Data and methods

Data

In this paper, 33 ChinArray II stations were selected to image the structure in the crust of the study area, and the observed cross-section spreads nearly east–west, including parts of the orogenic belt at the northern margin of the West Qinling, the Linxia block, the Longzhong block, the Liupanshan tectonic belt, and parts of the southwestern margin of the Ordos block. The 33 broadband seismic stations had an average interstation spacing of ~30 km, and all stations were equipped with a data acquisition system (Reftek 130) and a three-component broadband seismometer with a natural period of 60 s (Güralp CMG-3EPSC) or 120 s (Güralp CMG-3 T).

Extraction of P-wave receiver functions

P-wave receiver functions (PRFs) have become a relatively well-used method for studying crustal structures (Xu and Zhao, 2008; Chen et al., 2022). The PRF is extracted by separating the time series of the vertical component and the horizontal component from the records of the three-component broadband seismometer, and the vertical component and the horizontal component are deconvoluted to obtain a time series of the PRF that is well documented about the structure beneath the station (Langston, 1979; Ammon et al., 1990). The crustal structure below the station has a certain influence on the P-to-S conversion wave (Ps), so the Ps wave also records the structural information in the crust. Therefore, the PRF can be used to study the Moho structure, crustal structure, crustal thickness, and Poisson's ratio; the PRF can even be used to image the crust–mantle structure (Langston, 1979; Tian et al., 2005) and can also invert the crustal velocity structure (Liu et al., 1996). The current methods for extracting receiver functions mainly include iterative deconvolution in the time domain (Owens and Zandt, 1997) and deconvolution in the frequency domain (Langston, 1979). On this basis, the structure under the station is obtained through different technical methods.

The extraction of the PRF includes the following steps: first, download the earthquake catalogue combined with the station deployment time, select earthquake events according to the earthquake catalogue, convert the format of the original data, and intercept and select the seismic data at the same time. We select 439 seismic events of Ms ≥ 5.5 and epicentral distances between 30° and 90° that were recorded during the working hours of the array. The waveform data of the 20 s before and 100 s after the arrival of the P wave are intercepted (Figure 2) and then converted into sac format. Preprocessing, such as detrending and demeaning, is performed on the intercepted teleseismic waveform data. Then, we manually select the preprocessed data, and the data selection process is applied to CrazySeismic software (Yu et al., 2017). After
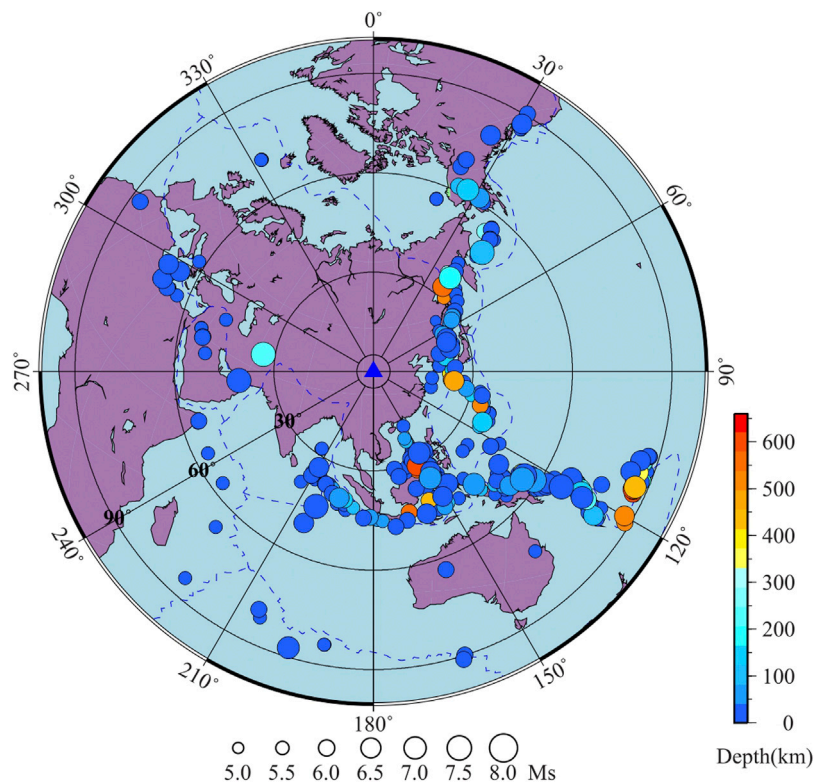
FIGURE 2
Distribution map of 439 teleseismic events in this study. Note that although some events are located inside the 30° and outside the 90° circle, all the seismograms that we used have an epicentral distance between 30° and 90°. (The colour code indicates the depth, and the size of the circle corresponds to the magnitude).

the preliminary selection, the three-component event waveforms are bandpass-filtered (two-pole Butterworth filter, with a corner frequency =0.05–2 Hz) and rotated from Z-N-E into Z-R-T components. Finally, based on the theory of equivalent seismic sources (Langston, 1979), the time domain deconvolution algorithm is used for calculation (Ligorria and Ammon, 1999), and the Gaussian filter factor is set to 2.5. Then, the extracted receiver function is further selected, and the data with a significant seismic phase of the P wave, clear seismic phase, and good consistency of Ps and PpPs are selected for the next imaging analysis. The receiver function results of stations 62,350 and 63,056 are shown in Figure 3, and the specific locations are marked in Figure 1. The results of the receiver function show that the quality of each available receiver function is good, the waveform information is clear, the seismic phase characteristics are clear, and the seismic propagation characteristics of the area are thus combined.

Common conversion point stacking (CCP)

The common conversion point stacking method (CCP) of the receiver function is developed based on the high-frequency ray approximate superposition theory. The high-frequency ray superposition method is the earliest-developed array receiver function imaging method (Chen et al., 2022). Dueker and Sheehan (1997) took the lead in introducing the idea of common midpoint superposition (CMP) of reflected waves into converted wave imaging of receiver functions. Through the given velocity model, the receiver function of oblique incidence is dynamically corrected and superimposed according to the relationship between the theoretical travel time and the incident angle, and finally, the interface fluctuation image under the array is obtained. Zhu and Kanamori (2000) made a further improvement on this basis and proposed the receiver function common conversion point superposition method (CCP). According to a given velocity model, the CCP superposition method back-projects each receiver function into the space domain according to the ray path and performs superposition imaging in the space domain (Zhu and Kanamori, 2000; Chen et al., 2022). The CCP superimposed imaging method has the advantages of high computational efficiency and a good horizontal medium imaging effect and has obvious advantages in revealing the interface between the crust and the upper mantle with broadband station data.

We used the Common Conversion Point (CCP) stacking method (Zhu and Kanamori, 2000) to image the crustal architecture beneath profile AA' (Figure 1B). The amplitudes of the RF waveforms were projected along the ray path of the conversion points based on a reference velocity model. The IASP91 model was selected for the time-depth conversion background velocity, and we fine-tuned the shallow velocity model according to the research results of previous
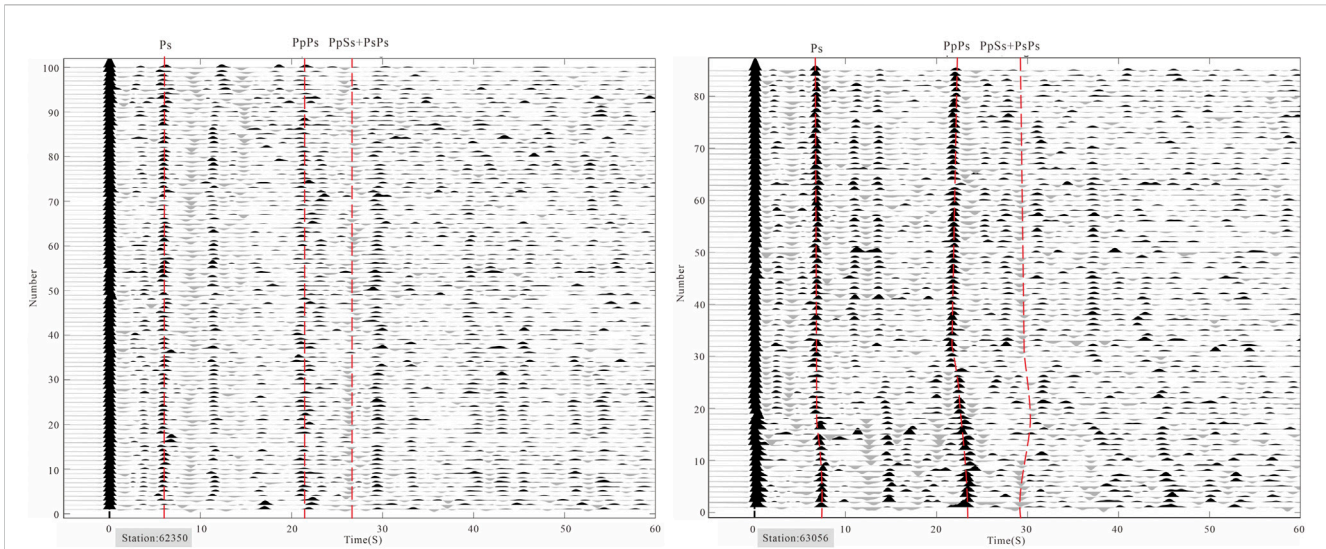
FIGURE 3
Receiver functions of stations 62,350 and 63,056. The horizontal axis is the delay time relative to the direct P wave. The vertical axis is the order number of the receiver functions, and the back azimuth gradually increases from bottom to top. The three red lines show the reference arrival times calculated with the IASPEI91 model for Ps, PpPs, and PpSs + PsPs.

researchers in the study area. In this paper, the three-dimensional P-wave and S-wave velocity models of the crust in the study area obtained by Ding et al. (2017) using the tomography method are selected to replace the velocities shallower than 50 km in the IASP91 model. The volume of the crust beneath the linear array was divided into bins with the sizes being 100 km wide, 35 km long, and 0.1 km thick. All the amplitudes in the same bin were stacked, averaged, and horizontally smoothed, and then the crustal structure was normalized with the amplitude distributions (Figure 6C).

H-κ stacking method

According to the theory of earthquake propagation, we know that the teleseismic P wave propagates from the mantle to the crust below the observation station, part of the P wave is projected there, and part of it is converted into an S wave and continues to propagate. The receiver function method is used to image the structure in the crust by enhancing the signal of this type of converted wave. In addition, the above two types of waves also undergo multiple reflections and propagations between the crust and the Moho interface, forming multiple waves, such as PpPs, PpSs, and PsPs. The expression of earthquake propagation is as follows:

$$
\begin{cases}
t_{\mathrm{P}} = H\sqrt{\dfrac{1}{V_{\mathrm{P}}^2} - p^2}, \\[2mm]
t_{\mathrm{S}} = H\sqrt{\dfrac{1}{V_{\mathrm{S}}^2} - p^2},
\end{cases}
\tag{1}
$$

Here, t_{P} and t_{S} in Formula 1 represent the travel times of the P wave and S wave in the layer with thickness H, respectively; V_{P} and

V_{S} represent the velocities of the P wave and S wave, respectively; p represents the ray parameter, which is $p = \frac{\sin i}{V_P}$; and i represents the incident angle of the P wave on the surface. According to Formula 1, the calculations of the travel times of various converted waves relative to the direct P wave can be obtained. The mathematical expression is as follows:

$$
\begin{cases}
t_{\mathrm{Ps}} = H\left(\sqrt{\dfrac{1}{V_{\mathrm{S}}^2} - p^2} - \sqrt{\dfrac{1}{V_{\mathrm{P}}^2} - p^2} \right), \\[3mm]
t_{\mathrm{PpPs}} = H\left(\sqrt{\dfrac{1}{V_{\mathrm{S}}^2} - p^2} + \sqrt{\dfrac{1}{V_{\mathrm{P}}^2} - p^2} \right), \\[3mm]
t_{\mathrm{PsPs+PpSs}} = 2H\sqrt{\dfrac{1}{V_{\mathrm{S}}^2} - p^2}.
\end{cases}
\tag{2}
$$

Formula 2 shows that the wave velocity ratio κ (Vp/Vs) is more sensitive to the crustal thickness than Vp, so to estimate the crustal thickness as accurately as possible, Zhu and Kanamori (2000) proposed the method of H-κ stacking. This method involves scanning and calculating H and κ within a certain range, bringing the searched H and κ into Formula 2 for calculation, and bringing the calculation results into objective function (3) for the solution:

$$
S(H, \kappa) = w_1 r(t_{\mathrm{Ps}}) + w_2 r(t_{\mathrm{PpPs}}) - w_3 r(t_{\mathrm{PsPs+PpSs}}),
\tag{3}
$$

Through the maximum value of the objective function obtained in Formula 3, the corresponding average crustal thickness and Vp/Vs ratio under the station can be obtained. By knowing the result of the Vp/Vs ratio, we can further obtain Poisson's ratio according to Formula 4. There is a linear relationship between the wave speed ratio and Poisson's ratio. The mathematical expression is as follows:

$$
\delta = 0.5 - \frac{1}{2\left(\kappa^2 - 1\right)}
\tag{4}
$$
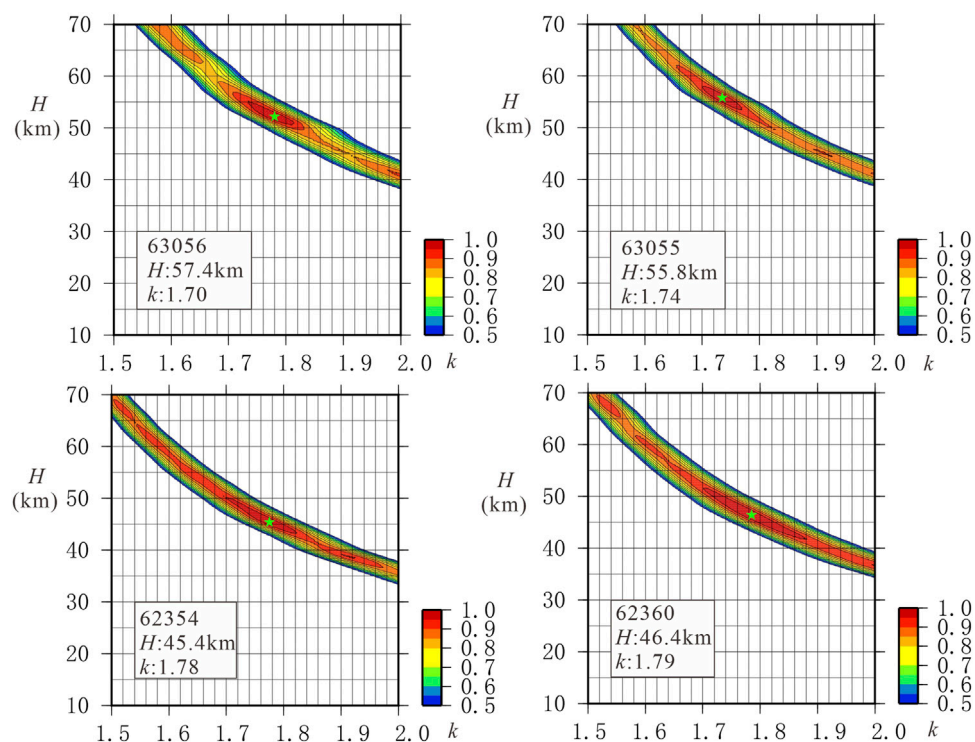
FIGURE 4
Results of H-κ stacking at stations 63,056, 63,055, 62,354, and 62,360. The vertical axis represents the thickness of the crust, the horizontal axis represents the wave velocity ratio, the best fitting point corresponds to the green pentagon, and the station number and corresponding crustal thickness and κ value are recorded in the small white box.

In the calculation process, we usually set the speed of the P wave as 6.3 km/s (Chen et al., 2005); the search interval of H is generally set to 20–70 km; the search interval of the κ value is generally set between 1.5 and 2.3; and the weighting coefficients of Ps, PpPs, and PpSs+PsPs multiples are set to 0.7, 0.2, and 0.1. Previous experience tells us that the value of the weighting coefficient has little effect on the calculation results (Tian et al., 2021).

Figure 4 shows the H-κ results under different stations in the study area. The figure shows that the weighted estimation point convergence effect is very good (green pentagonal heart), and the feasibility of the data is high.

Results

The results of previous studies show that the average crustal thickness of China is approximately 37 km, the average Poisson's ratio is approximately 0.25, the thickness of the Qinghai–Tibet Plateau is the thickest, and the average thickness is greater than 70 km (Chen et al., 2010; Teng et al., 2013; Gao et al., 2022). The average crustal thickness of the northeastern Qinghai–Tibet Plateau is approximately 50 ± 5 km (e.g., Gao et al., 2006; Tian and Zhang, 2013). Therefore, we adjust the depth of the Moho in the IASP91 model (Kennett and Engdahi, 1991) to 50 km and use this model as a reference to calculate the PS shock penetration point position and time-depth conversion calculation. The study area of this article is mainly in the eastern part of the western

Qinling Fault, as well as the Linxia block, Longzhong block, Liupanshan structure belt, and part of the southwestern edge of the Ordos block.

Crustal thickness

In this paper, the receiver functions of 33 stations in the study area were extracted by the above method. We used the iterative deconvolution method in the time domain (Ligorria and Ammon, 1999). This method has the advantages of stable calculation and clear receiver function waveforms. To suppress the influence of noise in the waveform data, the Gaussian filter factor is set to 2.5 in the receiver function calculation. Referring to previous research results (Gao et al., 2006; Li et al., 2006; Tong et al., 2007; Zhang et al., 2015; 2016; Tian et al., 2021), 6.2 km/s was selected as the average crustal velocity for superposition analysis, and the weighting coefficients of PpPs, PpSs, and PsPs multiples were set to 0.7, 0.2, and 0.1. We used the H-κ stacking method to obtain the crustal thickness (H) and the Vp/Vs ratio (κ) below each station. Due to the interference of different factors, such as data quality, venue conditions, and underground structure, the signal of the collection within some periods of individual stations is not good, for example, the data from station 62,363, the data from station 61,057 in 2015, and the data from stations 62,348 and 62,349 in 2014. Because the signal-noise-ratio of these stations is poor, they were discarded directly when the receiving function was selected.

Because there are many stations with better PRFs surrounding them, the deep structure of the research area is very good and has a high degree of credibility. Through efficient data selection by CrazySeismic software (Yu et al., 2017), PpPs, PpSs, and PsPs data with clear seismic phases and good theoretical travel times are selected, and the number of receiving functions obtained under each available station is approximately 150–280. The number of effective receiving functions under most stations is large, which ensures the reliability and representativeness of the results. Supplementary Table S1 shows the obtained H-κ results, and Figure 4 shows the H-κ superposition results of the four stations. The green pentagon in Figure 4 represents the best-estimated values of H and κ, the convergence effect is good, and there is no multiextreme value, indicating that the reliability of the data is high, and the station is marked by the numbers in the lower left corner and corresponding H and κ results. The average crustal thickness in the study area is 48.65 km, and the average Poisson's ratio is 0.25. From the northern margin of the West Qinling Fault to the southwest margin of the Ordos block, the Moho depth gradually changes from 57.6 km to 43.5 km, and the Moho below the Liupanshan fault zone has local depression characteristics. Previous survey results show that the thicknesses of the crust in the Liupanshan structural belt are approximately 45–50 km and has a high Poisson's ratio, while the thicknesses of the crust inside the Ordos block are approximately 42–43 km (Chen et al., 2005; Tong et al., 2007; Wang et al., 2014; Wang et al., 2017; Tian et al., 2021), which are consistent with our calculation results. The H-κ stacking results (Supplementary Table S1) and CCP stacking profiles (Figure 6) show that the crustal thickness in the study area gradually thins from the West Qinling fault to the southwestern margin of the Ordos block, but there is an obvious deformed depression feature in the Moho below the Liupanshan structural belt (Tong et al., 2007). In summary, our research results are consistent with previous research results in this area.
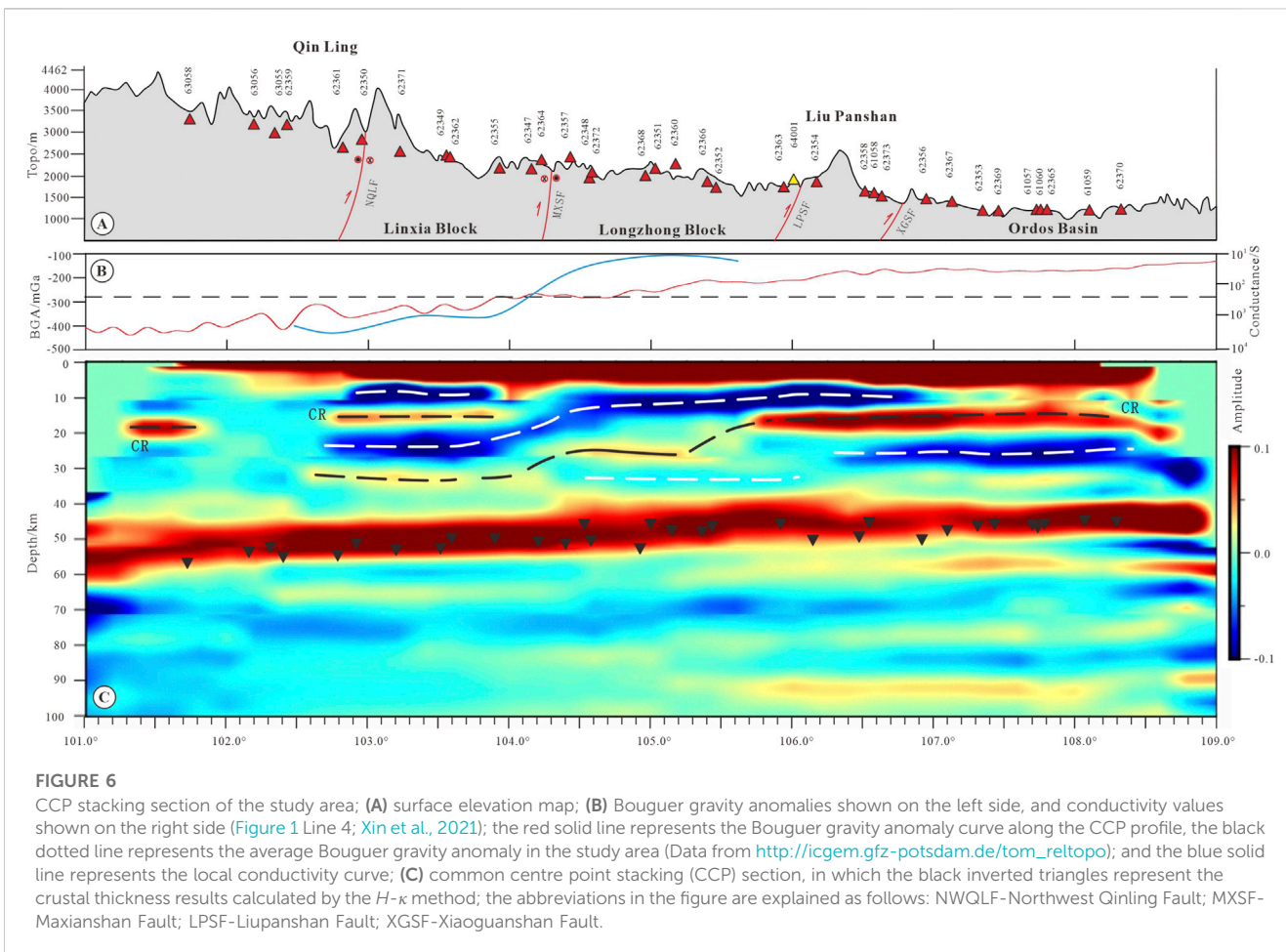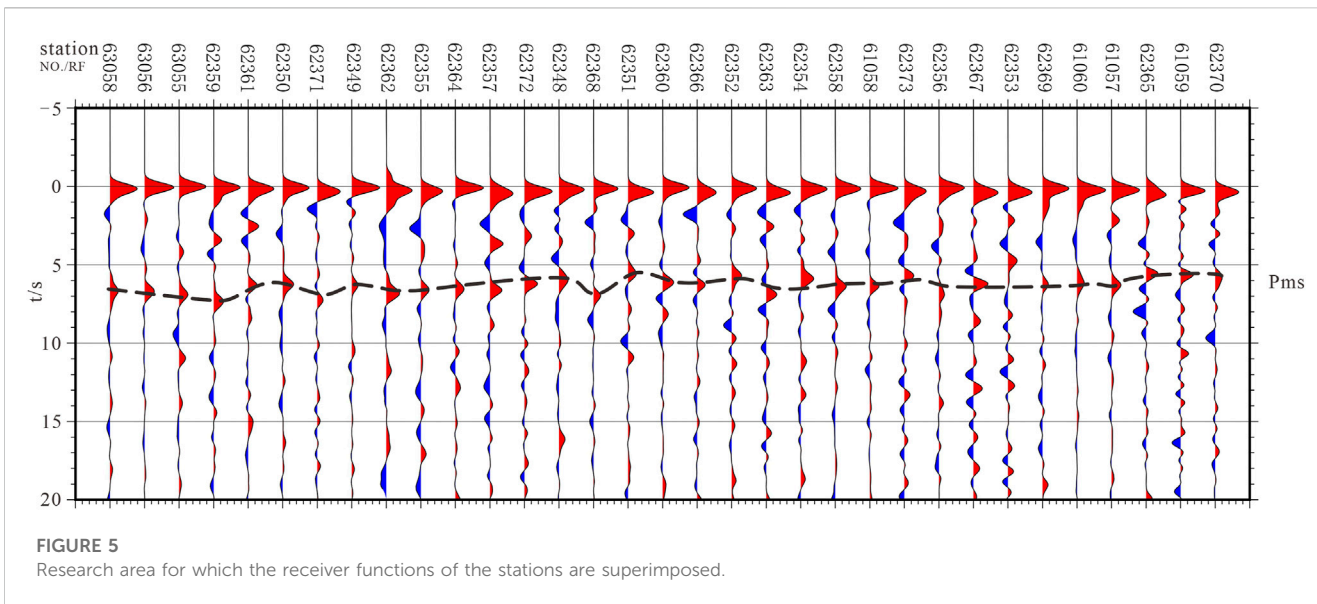
From Figure 6, we can conclude that the altitude gradually decreases from the West Qinling fault zone to the southwest margin of the Ordos block, and the Moho depth gradually decreases from 57.6 km to 43.6 km. The H-κ results (Supplementary Table S1) also correspond well. The Bouguer gravity anomaly has a good coupling relationship with the basin–mountain structure along the survey line. The red solid line in Figure 6B represents the Bouguer gravity anomaly curve in the study area, the numbers on the left represent the Bouguer gravity anomaly, and the numbers on the right represent the conductivity values. The black dotted line represents the average value of the Bouguer gravity anomaly. In general, the Bouguer gravity anomaly changes from small to large from west to east, and the lower part of the mountain range shows a relatively negative anomaly. There is good correspondence between the Qinling and the lower part of Liupanshan structural belt. The results of magnetotelluric inversion show that there are structural differences in the electrical conductivity between the Linxia block and the Longzhong block (Xin et al., 2021), as shown by the blue line in Figure 6B. The Linxia block has high conductance, while the Longzhong block has low conductance. The rate of conductivity change in the Maxianshan fault is the highest, and the above evidence indicates that the Maxianshan fault is the suture line between the Linxia block and the Longzhong block.

Crustal structure

Through the analysis of CCP sections (Figure 6C), we believe that the study area has obvious difference between adjacent blocks. From west to east is the Qinling orogenic belt, Linxia block, Longzhong block, and Ordos block. The layered interface below the Qinling orogenic belt is poor, and the amplitude in the crust is weak (Figures 5, 6C), which may be related to the tectonic movement of the Northwest Qinling Fault (NWQLF) that has undergone multiple periods of strike-slip and thrusting structural deformation (Zhang and Ding, 1996; Cheng et al., 2003; Zhan et al., 2004), and complex tectonic activities destroyed the inner shell structure. The layered interface within the crust of the Linxia block between the Northwest Qinling Fault (NWQLF) and the Maxianshan Fault (MXSF) is visible (Figure 6). Between 102.8° and 103.9°, there are two continuous positive seismic phase boundaries at depths of ~18 km and ~32 km, and we speculate that the shallow normal seismic phase boundary is the Conrad boundary (CR). There are two obvious negative seismic phase boundaries above and below the CR, which are located at depths of ~8 km and ~25 km, respectively.

The crustal structures of the Longzhong block and the Linxia block are significantly different. There is a continuous negative seismic phase in the upper crust of the Longzhong block approximately 10 km away, it enters the southwest margin of the Ordos block through the Liupanshan Fault and the Xiaoguanshan Fault, and the CR is not developed. A weaker positive seismic phase develops at a depth of approximately 25 km, and a weaker negative seismic phase develops in the lower crust. The lateral interface between the Longzhong block and the Linxia block shows an obvious discontinuous feature, and there is an obvious negative seismic phase transition from west to east that shallows from 20 km to 10 km, which may be the deep manifestation of the Maxianshan fault as a boundary fault in the middle and upper crust. Previous receiver functions and their linear inversion results suggest that there is a dividing line between the Qinling Mountains and the Qilian Mountains at 105°E in the Longxi Basin (Liu et al., 2008b); however, it is evident only from the S-wave velocity, and the deep distribution of this boundary is not proposed. We believe that the continuous west-dipping negative seismic phase (104°–104.5°) below the Maxianshan fault zone in the CCP imaging results is the location of the ancient suture line between the Longzhong block and the Linxia block. This conclusion is consistent with the research results of magnetotelluric (MT) and deep seismic reflection profiles (Guo et al., 2016; Xin et al., 2021). There is a continuous negative seismic phase boundary with a length of ~250 km at a depth of 10 km between the Maxianshan fault and the Xiaoguanshan fault, which may be deep evidence of the local overall uplift of the Longzhong block and its extension to the Ordos block. Because the surface along the southeast of the Maxianshan Fault in the study area is covered by thick and near-horizontal sedimentary layers and the faults are not developed, the research level of this area is relatively low, but the Cenozoic strata have obvious structural characteristics of overall uplift (Guo et al., 2018a), so our CCP imaging results have a good correspondence with the geological phenomenon of regional uplift.

There is an obvious discontinuity of the transverse velocity interface under the Liupanshan structural belt. The negative seismic phase at ~10 km shows a tendency to expand eastwards;

FIGURE 5
Research area for which the receiver functions of the stations are superimposed.

FIGURE 6
CCP stacking section of the study area; **(A)** surface elevation map; **(B)** Bouguer gravity anomalies shown on the left side, and conductivity values shown on the right side (Figure 1 Line 4; Xin et al., 2021); the red solid line represents the Bouguer gravity anomaly curve along the CCP profile, the black dotted line represents the average Bouguer gravity anomaly in the study area (Data from http://icgem.gfz-potsdam.de/tom_reltopo); and the blue solid line represents the local conductivity curve; **(C)** common centre point stacking (CCP) section, in which the black inverted triangles represent the crustal thickness results calculated by the *H-κ* method; the abbreviations in the figure are explained as follows: NWQLF-Northwest Qinling Fault; MXSF-Maxianshan Fault; LPSF-Liupanshan Fault; XGSF-Xiaoguanshan Fault.

there is a discontinuous positive seismic phase boundary at ~15 km depth; and the negative seismic phase at a depth of ~18 km is relatively continuous in the Ordos block (Figure 6C). The layered structure in the deep part of the Ordos block is better, the crustal deformation is weaker, and it has the characteristics of an ancient cratonic base. There is an obvious positive seismic phase at ~15 km, which we believe is the Conrad boundary (CR) of the Ordos block. There is a continuous Conrad interface of approximately 18–20 km in the northwest margin

of the Ordos block (Chen et al., 2020), which reflects the characteristics of a stable craton with good stratification in the Ordos crust (Chen et al., 2005; Tian et al., 2021; Chen et al., 2022). The velocity discontinuity below the Liupanshan fault zone shows a discontinuous west-dipping trend, which may be controlled by the multiple thrust nappe structures of the Liupanshan fault; the deep structure is relatively broken and is characterized by a west-dipping and eastwards thrust towards the Ordos block.

Poisson's ratio results

Poisson's ratio (σ) is one of the important parameters for studying the crustal structure, its range of variation is related to the rock composition and type, and the continental crustal material composition is related to Poisson's ratio (Christensen, 1996). Among the crustal material components, as the SiO_2 content increases, Poisson's ratio decreases. The Poisson's ratio of acidic rocks with felsic contents as the main component is $\sigma \leq 0.26$, the Poisson's ratio of neutral rocks is $0.26 < \sigma \leq 0.28$, and the mafic–basic rocks are $0.28 < \sigma \leq 0.3$. If the Poisson's ratio $\sigma > 0.3$, the study area may be a tectonic fracture zone, the area may have a fracture undergoing strong serpentinization, or it may be experiencing regional partial melting (Ji et al., 2009; Gong et al., 2015). We calculated the obtained H-k results by formula (4) to obtain the Poisson's ratio (σ) below each station, and the calculation results are shown in Supplementary Table S1. Through the method of linear interpolation, we obtained the average crustal Poisson's ratio distribution results in the study area (Figure 7). The Poisson's ratio results (Supplementary Table S1; Figure 7) show that the overall Poisson's ratio in the study area is low, and the average Poisson's ratio in the study area is 0.26, but there are local high Poisson's ratio anomalies in the Longzhong block and Linxia block (Figure 7). The Poisson's ratio of the North Qinling fault zone and its adjacent areas is small, ranging from 0.21 to 0.25, but the Poisson's ratio of station 62,359 is 0.28, showing a local anomaly, which may be related to its deep structural fragmentation. The Poisson's ratios of the Linxia block range from 0.24 to 0.29, and the Poisson's ratios of 50% of the stations are less than 0.26. There are small-scale elliptical high Poisson's ratio anomalies (Figure 7), which may indicate that a small amount of oceanic basalt is preserved in its deep crust. The distribution area of high Poisson's ratio anomalies in the Longzhong block is relatively large, and Poisson's ratios range from 0.24 to 0.31, showing an M-shaped east–west distribution (Figure 7). This distribution may be due to the preservation of the oceanic crust basalt composition after the subduction of the oceanic crust. As a component of the ancient craton, the Ordos block has a lower Poisson's ratio overall.

Discussion

Differences in the crustal structure of the Linxia block, Longzhong block, and Ordos block

The Maxianshan fault is an important boundary fault that divides the Linxia block and the Longzhong block. The Linxia block has an obvious layered structure in the crust, a developed

Conrad interface, and low-velocity anomalies in the middle and lower crust, which may contain saline fluid (Jin et al., 2012) and have the characteristics of a Japanese-type island arc (Guo et al., 2016; Xin et al., 2021). The layered structure of the upper crust in the Longzhong block is obvious, the layered structure of the middle and lower crust is weak and presents weak low-velocity characteristics, the Conrad interface is not developed, and it has the characteristics of ocean-island basaltic crust. The Longzhong block may have been formed by Mariana-type island arcs (Guo et al., 2015). The Conrad interface and the Moho lateral variation in the southwestern margin of the Ordos block are weak, showing the characteristics of a stable craton. The Liupanshan tectonic belt is an important boundary fault that divides the Longzhong block and the Ordos block.

A large number of geophysical research results show that the Linxia block and the Longzhong block are important components of the eastern part of the Qilian Mountain orogenic belt (Gao et al., 2011; Jin et al., 2012; Guo et al., 2016). The tectonic evolution of the eastern section of the Qilian Mountain orogenic belt is complex. The late Palaeozoic–early Mesozoic experienced a complex tectonic evolutionary process in which the Qilian Ocean was closed and different blocks merged. During the Late Ordovician–early Silurian, the Linxia block of the Japanese-type island arc and the Longzhong block of the Mariana-type island arc were spliced together due the closure of the Qilian Ocean (Cheng et al., 2016; Xin et al., 2021). The Maxianshan Fault and the Liupanshan Fault, as the dividing line between different blocks, played an important restrictive role in late Mesozoic and Cenozoic tectonic shortening and plateau uplift. The Hezuo–Dajing profile of Jin et al. (2012) resolved a conductive layer in the crust corresponding to partial melt and saline fluids. Xia et al. (2019) resolved a structure consisting of several irregular high-resistivity blocks and low-resistivity layers in the crust, which were thought to be the sources of the earthquakes in this region. The middle and lower crust of the Linxia block is characterized by low-resistivity anomalies, while the upper crust is dominated by high-resistivity anomalies (Xin et al., 2021). The results of the deep seismic reflection profile show that the Linxia block has developed obvious extrusive fold deformation (Guo et al., 2016). Therefore, we speculate that the high-conductivity and low-velocity structure of the lower crust of the Qinling orogenic belt and the Linxia block may be caused by structural fragmentation caused by multistage tectonic deformation and filled with salinized fluids. The study area is affected by the remote effect of the collision between the Indian continent and the Eurasian continent, and the seismic sources of the Linxia block are mostly distributed in the upper crust (Xin et al., 2021), which may be because the rigid upper crust more easily stores and releases energy, thus triggering earthquakes; in addition, the existence of high-conductivity, low-velocity bodies in the middle and lower crust is more likely to cause ductile deformation and vertical thickening. The Japanese-type island arc is a product of oceanic and continental subduction. The oceanic crust below the continental plate subducts to the side of the continental margin. It is often the product of a compressional collisional environment. The dehydration of the subducted oceanic crust generally leads to partial melting or upwelling of the upper mantle material. According to the MT results, there is a high-
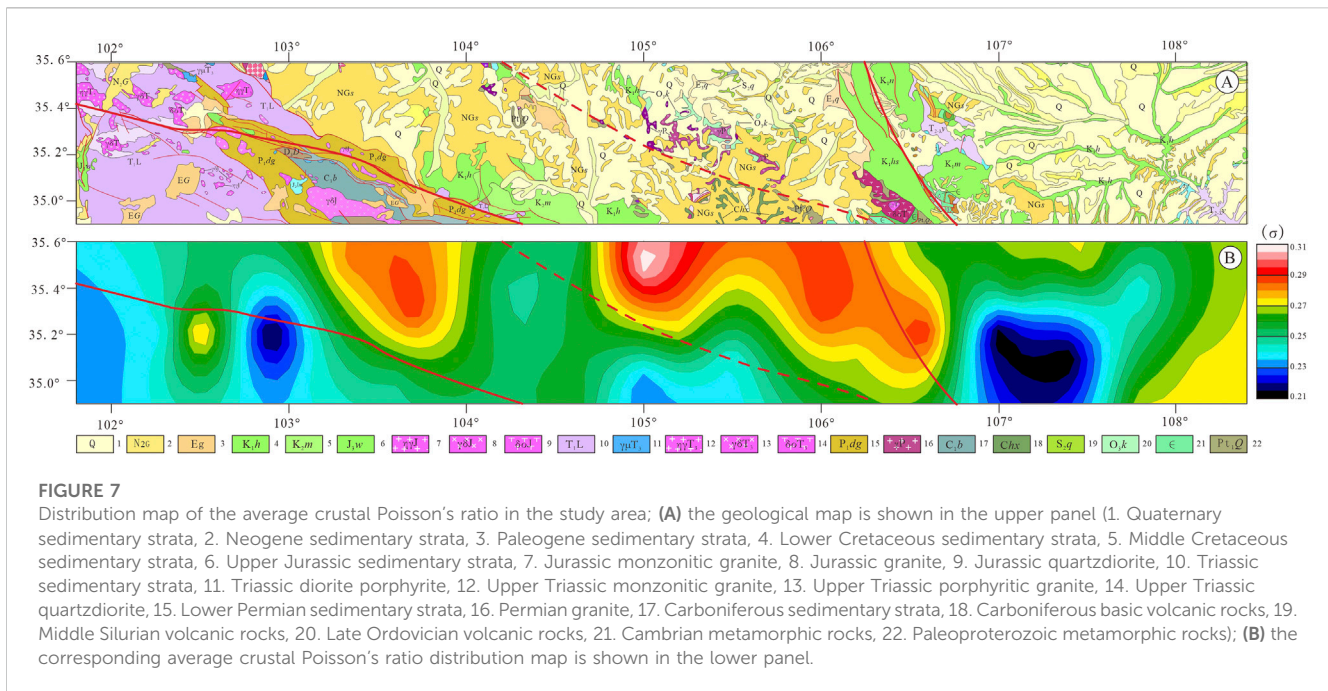
FIGURE 7
Distribution map of the average crustal Poisson's ratio in the study area; **(A)** the geological map is shown in the upper panel (1. Quaternary sedimentary strata, 2. Neogene sedimentary strata, 3. Paleogene sedimentary strata, 4. Lower Cretaceous sedimentary strata, 5. Middle Cretaceous sedimentary strata, 6. Upper Jurassic sedimentary strata, 7. Jurassic monzonitic granite, 8. Jurassic granite, 9. Jurassic quartzdiorite, 10. Triassic sedimentary strata, 11. Triassic diorite porphyrite, 12. Upper Triassic monzonitic granite, 13. Upper Triassic porphyritic granite, 14. Upper Triassic quartzdiorite, 15. Lower Permian sedimentary strata, 16. Permian granite, 17. Carboniferous sedimentary strata, 18. Carboniferous basic volcanic rocks, 19. Middle Silurian volcanic rocks, 20. Late Ordovician volcanic rocks, 21. Cambrian metamorphic rocks, 22. Paleoproterozoic metamorphic rocks); **(B)** the corresponding average crustal Poisson's ratio distribution map is shown in the lower panel.

resistance upper crust in the Linxia block, and the middle and lower crust have the characteristics of high-low conductivity interlayers (Xin et al., 2021), which correspond well to our CCP results (Figure 6C). In the Cenozoic, due to the joint control of the Maxianshan fault and the fault at the northern margin of the West Qinling, the Cenozoic sedimentary strata in the Linxia Block were nearly horizontal. However, due to the shortening of the NE-trending structure on the northeastern margin of the Qinghai–Tibet Plateau, overall uplift occurred, resulting in the loss of Quaternary strata (Guo et al., 2016). In summary, we believe that the crustal layered structure of the Linxia block is obvious, and the low-velocity layer of the lower crust is developed. This low-velocity layer may represent the ductile deformation area of the middle–lower crust caused by the subduction of the Qilian Ocean crust, which contains saline fluids. In the Mesozoic–Cenozoic, this area experienced multiple stages of structural shortening deformation, and the upper crust was dominated by thrust napping and shortening deformation (Darby and Ritts, 2002). This thrust nappe structure corresponds well with the low-velocity layers of the upper crust of the Linxia block and the Longzhong block (Figure 6C). The middle–lower crust is dominated by ductile deformation with lateral shortening and longitudinal thickening.

The P-wave receiver function method is more sensitive to horizontally layered velocity discontinuities in the crust, the layered structure of the whole crust is present in the Linxia block, and the CR is developed. However, the layered structure of the upper crust of the Longzhong block is obvious, the layered interface of the middle and lower crust is not developed, and the CR is not developed. The MT research results indicate that the Longzhong block shows a high-resistance anomaly (Figure 6B; Xin et al., 2021). We believe that the high-resistivity body with no layered structure in the middle and lower crust of the Longzhong block may be related to oceanic island basalts during the formation

of Mariana-type island arcs, which are the result of oceanic lithosphere subduction beneath oceanic plates and are characterized by widespread basalts (Hart et al., 1972). In summary, we believe that the Linxia block and the Longzhong block have different crustal and electrical structures, mainly because the Linxia block and the Longzhong block belong to different blocks. The Linxia block may have originally belonged to the continental margin of the Qaidam–Qilian block, which formed a Japanese-type island arc due to the subduction of the Qilian Ocean. The Longzhong block belongs to the Mariana-type island arc that formed during the subduction of the oceanic plate. With the closure of the Qilian Ocean, the Maxianshan fault became the collisional boundary of these two ancient island arcs and now exists in the form of the Maxianshan fault. The mafic dikes found in the Maxianshan Group record this splicing process (He et al., 2008). Our research results show that there are obvious differences in the crustal structures of the Linxia block and the Longzhong block on both sides of the Maxianshan fault (Figure 6). The research results of rock geochemistry (Xiao et al., 2009), MT profiles (Xin et al., 2021) and deep seismic reflection profiles (Guo et al., 2016) all support our conclusion.

In summary, the results of seismic detection and MT research show that there are obvious differences in the crustal structure between the Linxia block, the Longzhong block, and the Ordos block. The layered structure of the upper crust in the Longzhong block is developed, but the layered velocity discontinuity of the middle and lower crust is not developed, and it may be composed of Mariana-type island arcs; the layered structure of the Linxia block is developed, and the Conrad interface is developed. The middle and lower crust have obvious low-velocity and high-conductivity anomalies, which may contain saline fluid and have the characteristics of Japanese-type island arcs. As the boundary fault between the Linxia block and the Longzhong block, the Maxianshan fault has obvious sharp changes in the seismological structure and electrical conductivity. The

Haiyuan–Liupanshan fault zone has well-developed thrust nappe structures and frequent seismic activities, which may represent the collisional and splicing boundary between the Ordos block and the Longzhong block (the Mariana-type island arc) on the western margin of the North China block.
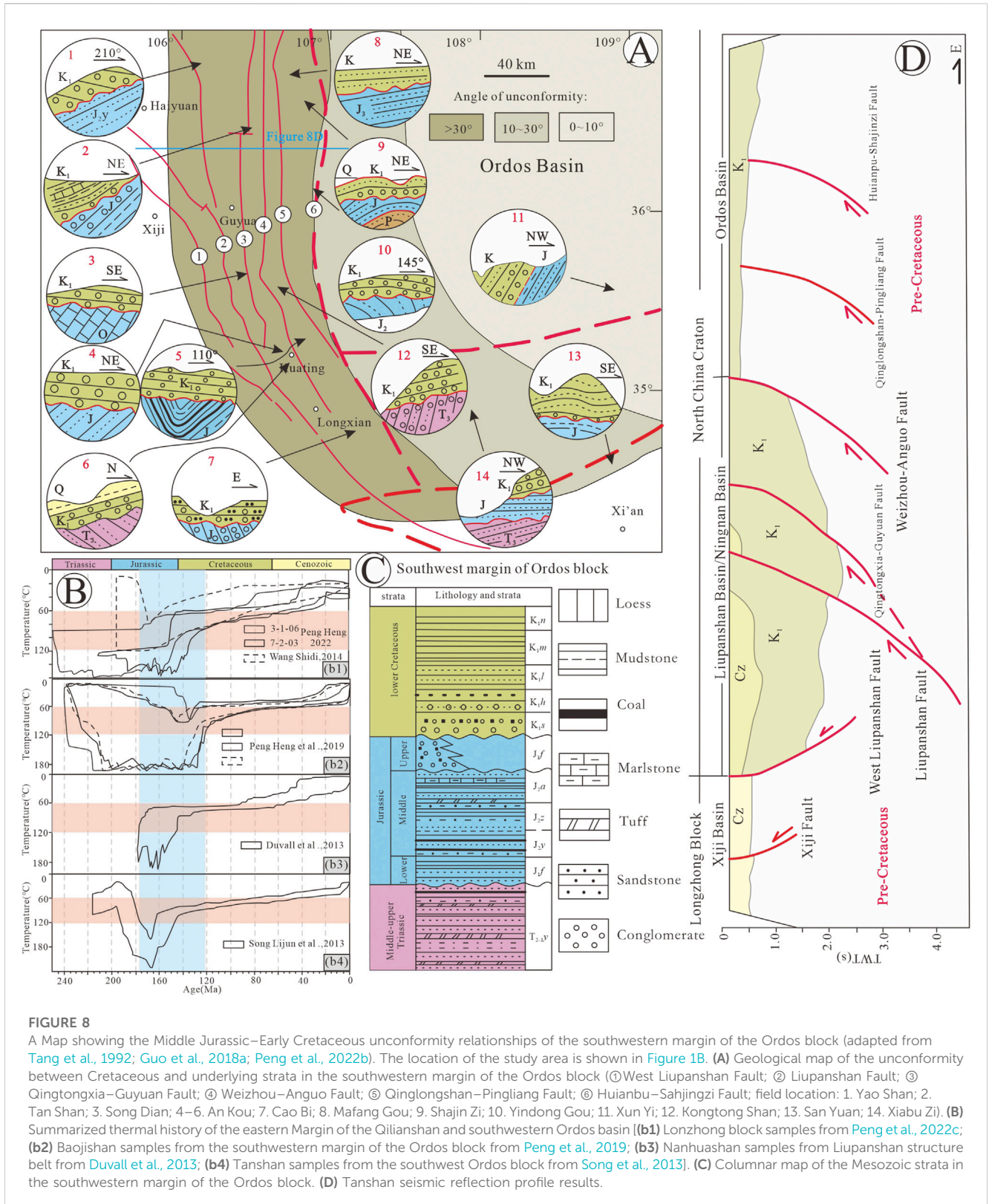
Structural evolutionary history

The eastern segment of the Qilian orogenic belt is composed of the Linxia block and the Longzhong block, which is now represented by the geomorphic features of the basin. It is located at the forefront of the northeastern margin of the Qinghai–Tibet Plateau, comprising a "rhombic-shaped area" controlled by multiple large, deep boundary faults, where the Qilian–Qaidam, western Qinling, Alxa, and Ordos blocks meet (Song et al., 2006; Figures 1A,B). The Haiyuan and Tianjingshan faults control the contact between the Longzhong block and the Alxa block. The Longzhong block is connected to the Ordos block in the east and divided by the Liupanshan fault. The western Qinling northern margin fault is the boundary between the Linxia block and the western Qinling block (Figure 1A). The Maxianshan fault system, where a pillow-shaped basaltic rock belt is exposed, forms a boundary between the Linxia block and the Longzhong block (Figure 1B). This typical suture mark implies that the Maxianshan fault is an important structural boundary separating the Linxia block and the Longzhong block (Pei et al., 2006; Xin et al., 2021). From the early Palaeozoic to the Mesozoic, the area experienced the collision and splicing of the North China plate and the Qilian–Qaidam block, corresponding to the subduction and closure of the Qilian Ocean's crust (Wu et al., 1993; Xu et al., 1994; Yang et al., 2002; Song et al., 2006). Evidence from geochemical, chronological, and field geological surveys shows that this area experienced significant crustal shortening and thickening events during the Late Triassic–Early Cretaceous (Lin et a, 2011; Dong and Santosh, 2016; Peng et al., 2018; 2019). Influenced by the uplift and expansion of the Qinghai–Tibet Plateau in the Cenozoic, the study area also experienced differential uplift and orogeny. In summary, it is of great scientific significance to clarify the deep structural and evolutionary processes of the northeastern margin of the Qinghai–Tibet Plateau through our research results and combined with previous geochemical and geochronological results.

The closure and collision of the Qilian Ocean occurred between the Alxa block and the Qaidam–Qilian block (Yin and Harrison, 2000; Gehrels et al., 2003; Song et al., 2013). The Qilian Ocean expanded in the late Palaeozoic and late Cambrian and began to subduct in the early Ordovician, forming island arcs and back-arc basins (corresponding to the Longzhong block and Linxia block). During the Late Ordovician–early Silurian, the Qilian Ocean began to close (Cheng et al., 2016). The North Qilian fold belt formed during the Caledonian orogeny, and many ophiolites, subduction zone-related complexes, and high-pressure metamorphic rocks were exposed in the suture zone (Xu et al., 1994; Song et al., 2013; Andrew et al., 2019). The location of this suture in the western part of the North Qilian orogenic belt is relatively clear (Figure 1B; Xu et al., 1994); however, there are few studies on the closure location, closure method, and suture zone location of the Qilian Ocean in the eastern segment of the Qilian orogenic belt (Figure 1B).

The North Qilian fold belt was formed during the Caledonian orogenic period, and its western section is composed of ophiolites, subduction complexes, and high-pressure metamorphic belts, representing the suture location of the Qaidam–Qilian block and the North China block (Xu et al., 1994; Song et al., 2013; Andrew et al., 2019). Although the MT research results across the Liupanshan Mountains show that there is a trench–arc–basin system in the eastern segment of the Qilian orogenic belt, which may correspond to the subduction and closure of the palaeo-ocean in the study area (Han et al., 2016), the suture location, closure method and geological evidence of the Qilian Ocean in the eastern section of the Qilian Mountain orogenic belt are still unclear (Figure 1). The MT research results show that with the Maxianshan fault as the boundary, there are obvious differences in electrical structure between the Linxia block and the Longzhong block (Xin et al., 2021). Our receiver function research results also show significant differences in the crustal structure between the Linxia block and the Longzhong block (Figures 6, 7). Field geological surveys have found that there are a large number of basic complex rocks in the Maxianshan rock group (He et al., 2008). These basic complex rocks were emplaced in the early Silurian and are considered to be important evidence of tectonic magma in the eastern part of the middle Qilian orogenic belt (Cheng et al., 2016), which was likely in place when the early Silurian Qilian Ocean closed. These basic complexes may have also been formed by the upwelling or overflow of mantle material during the subduction of the oceanic crust below the continental margin of the Qaidam–Qilian block. Its formation and emplacement may be related to the subduction and closure of the Qilian Ocean, or it may be a basic complex formed by the upwelling of mantle materials during the closure of the Qilian Ocean (Figure 9A). Altogether, this evidence suggests that mafic rocks are closely related to the subduction and closure of the Qilian Ocean (Cheng et al., 2016). Therefore, the Maxianshan fault located between the Linxia block and the Longzhong block represents the closure boundary of the Qilian Ocean in the eastern segment of the Qilian orogenic belt. In summary, the Linxia block has the characteristics of Japanese-style island arcs, and the Longzhong block is composed of the original Qilian Ocean Mariana-type island arc. The results of MT and deep seismic reflection profiles have revealed this attribute (Guo et al., 2015; Xin et al., 2021).

Significant crustal thickening and rapid uplift occurred in the eastern segment of the Qilian orogenic belt in the Mesozoic and Middle Jurassic–Early Cretaceous (Darby and Ritts, 2002; Dong and Santosh, 2016; Peng et al., 2021; Cheng et al., 2022). Through the collection of previous geological survey data, we drew a comprehensive map of the contact relationship between the Cretaceous strata and the underlying strata in the southwestern margin of the Ordos Basin and a columnar map of the Liupanshan belt (Figures 8A, C). From Figure 8A, it can be concluded that the western margin of the basin has a high-angle unconformity relationship, and the unconformity angle gradually decreases when entering the interior of the basin to the east, indicating that the structural deformation intensity gradually decreases. On the western margin of the Ordos Basin, the Cretaceous strata cover the Jurassic, Triassic, and Palaeozoic strata; inside the basin, the Cretaceous strata cover the Jurassic strata (Figure 8D; Guo et al., 2018b), which shows that from the interior of the basin to the eastern edge of the Qilian orogenic belt, the denudation intensity of the

FIGURE 8
A Map showing the Middle Jurassic−Early Cretaceous unconformity relationships of the southwestern margin of the Ordos block (adapted from Tang et al., 1992; Guo et al., 2018a; Peng et al., 2022b). The location of the study area is shown in Figure 1B. **(A)** Geological map of the unconformity between Cretaceous and underlying strata in the southwestern margin of the Ordos block (①West Liupanshan Fault; ② Liupanshan Fault; ③ Qingtongxia−Guyuan Fault; ④ Weizhou−Anguo Fault; ⑤ Qinglongshan−Pingliang Fault; ⑥ Huianbu−Sahjingzi Fault; field location: 1. Yao Shan; 2. Tan Shan; 3. Song Dian; 4−6. An Kou; 7. Cao Bi; 8. Mafang Gou; 9. Shajin Zi; 10. Yindong Gou; 11. Xun Yi; 12. Kongtong Shan; 13. San Yuan; 14. Xiabu Zi). **(B)** Summarized thermal history of the eastern Margin of the Qilianshan and southwestern Ordos basin [**(b1)** Lonzhong block samples from Peng et al., 2022c; **(b2)** Baojishan samples from the southwestern margin of the Ordos block from Peng et al., 2019; **(b3)** Nanhuashan samples from Liupanshan structure belt from Duvall et al., 2013; **(b4)** Tanshan samples from the southwest Ordos block from Song et al., 2013]. **(C)** Columnar map of the Mesozoic strata in the southwestern margin of the Ordos block. **(D)** Tanshan seismic reflection profile results.

strata gradually enhances. This deformation and exhumation process occurred in the Middle−Late Jurassic−Early Cretaceous (Figures 8A, B; Guo et al., 2018b; Zhao et al., 2019; Peng et al., 2022a). The results of the two-dimensional seismic section across

the Liupanshan structural belt show that two west-dipping thrust faults do not cut through the Cretaceous strata (Figure 8C), which indicates that the Liupanshan fault zone was active before the Cretaceous. Sedimentological and structural geological studies
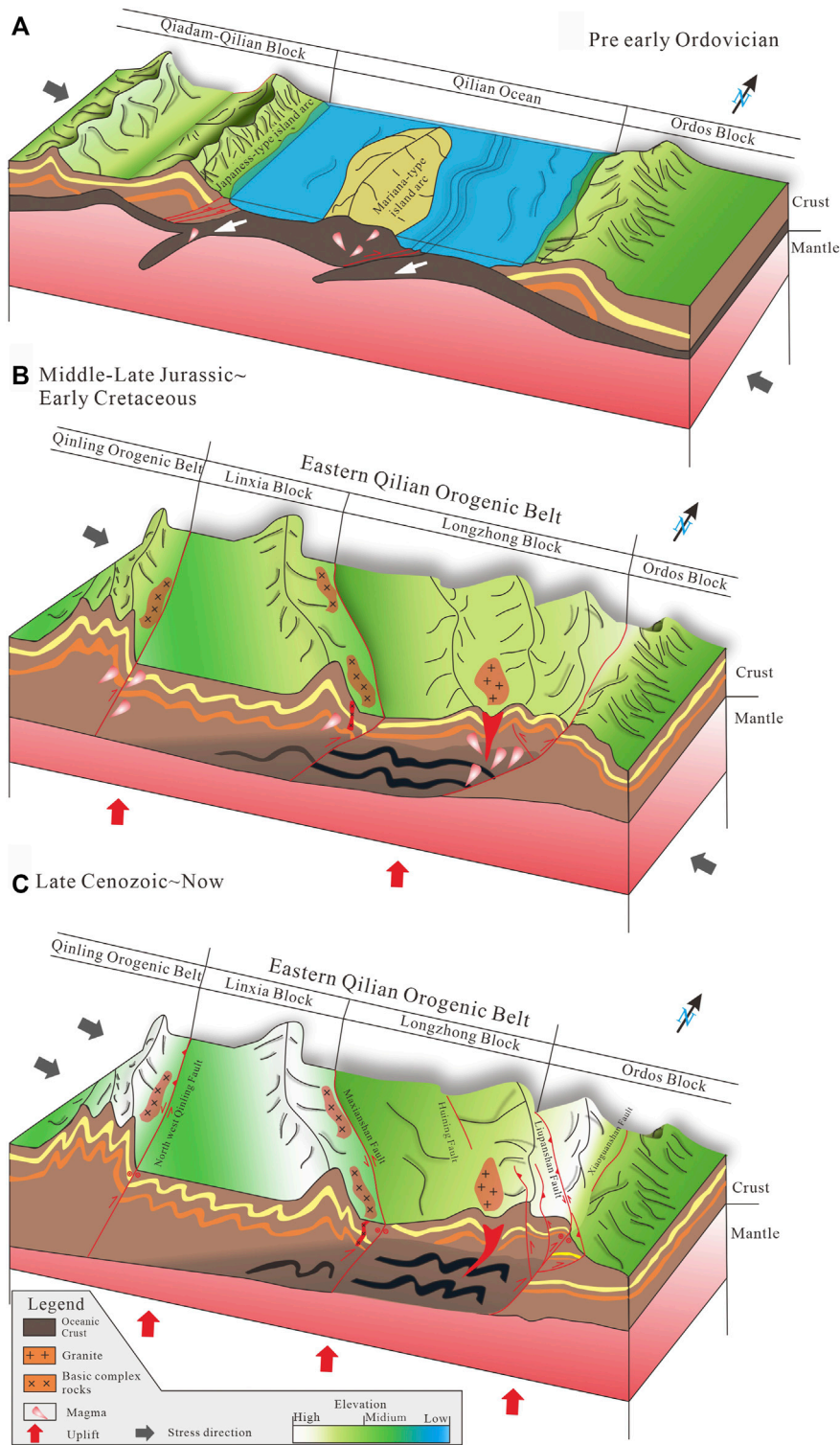
FIGURE 9
Structural evolutionary model diagram. **(A)** The closure model of the Qilian Ocean in the study area before the Early Ordovician; **(B)** the lithospheric crustal shortening and thickening processes in the Late−Middle Jurassic−Early Cretaceous; **(C)** the growth and expansion of the plateau since the late Cenozoic in the northeastern margin of the Qinghai−Tibet Plateau.

have shown that the western margin of the Ordos block has strong thrust nappe deformation, which was the thrust nappe of the East Qilian orogenic belt in the Middle Jurassic–Early Cretaceous (Darby and Ritts, 2002; Liu et al., 2005; Wang et al., 2019; Cheng et al., 2020). Apatite fission track (AFT) results show that the Longzhong block experienced a significant rapid cooling event in the Middle

Jurassic–Early Cretaceous (~174–120 Ma) (Figure 8B; Peng et al., 2019; Peng et al., 2022a; Duvall et al., 2013; Song et al., 2013). The simulation results show that the temperature of minerals has dropped by 60°C–80°C, and the palaeo geothermal gradient of 40°C/km is used as the estimate (Ren et al., 2005; 2017) since the Middle Jurassic–Early Cretaceous Qilian orogenic belt retreated 1.5–2 km (Peng et al., 2022c) to the east; this retreat was the main stage of crustal shortening in the northeastern margin of the Qinghai–Tibet Plateau, and the tectonic deformation events in this period are generally developed in the Qinghai–Tibet Plateau and its periphery (Kapp et al., 2007; Zhu et al., 2016; Dong et al., 2018). In summary, strong crustal shortening occurred in the study area during the Middle Jurassic–Early Cretaceous (~174–120 Ma), low-velocity layers in the middle and lower crust mainly developed within the ductile shortening deformation, and the upper crust is dominated by brittle shortening deformation of thrust napping (Liu et al., 2005; Liu et al., 2006; Wang, 2007). This tectonic event led to the differential uplift of the Linxia block and the Longzhong block, and the Longzhong block thrusted and napped on the western edge of the Ordos block (Figure 9B).

The late Cenozoic tectonic evolution of the northeastern margin of the Qinghai–Tibet Plateau is generally believed to have occurred along a series of active faults, such as the Haiyuan fault, the Liupanshan fault, and the Maxianshan fault (Zheng et al., 2010; Duvall et al., 2013; Peng et al., 2022b). The results of low-temperature thermochronology show that Nanhuashan experienced rapid uplift at 12 ± 3 Ma (Lin et al., 2010; Wang et al., 2014). The northern section of Yueliangshan experienced rapid uplift at approximately 7 Ma (Peng et al., 2019). From 7.3 to 8.2 Ma, the eastern section of the Haiyuan fault zone and the hanging wall of the Liupanshan thrust–nappe structural belt experienced significant uplift (Zheng et al., 2006; Zhao et al., 2007). All the above evidence indicates that the Haiyuan–Liupanshan fault zone was gradually activated during 15–7 Ma (Zheng et al., 2006; Zhao et al., 2007; Wang W. et al., 2013). However, the AFT of the Longzhong block showed that no significant structural uplift occurred during 15–7 Ma (Figure 7B; Peng et al., 2022c), which means that the rapid uplift event during 15–7 Ma was limited to the local uplift of the Haiyuan–Liupanshan fault zone. That is, the coastal Yuan-Liupanshan fault zone in the eastern section of the Qilian orogenic belt experienced northeast–nearly east–west peripheral expansion and plateau growth. Due to the limitation of the North China plate and the limited deformation space, it is speculated that Cenozoic structural deformation mostly occurred in the reactivated Late Jurassic structure, indicating that the preexisting structure controlled the Late Cretaceous–Cenozoic deformation activities. The results of MT research across the Madongshan–Liupanshan structural belt show that there are several low-resistivity striped positive flower structures under the high-resistivity background of the southwestwards-dipping strata under the Longzhong block (Zhan et al., 2017). Seismic reflection sections across the Niushoushan–Luoshan fault zone also reveal evidence of the existence of an upper crustal positive flower structure (Wang Q. et al., 2013). Our imaging results show that the thrust nappe deformation zone of the upper crust of the Longzhong Block (low-velocity layer of the upper crust, Figure 6C) passed through the Liupanshan tectonic belt and entered the southwestern margin of the Ordos Block. Since the late Cenozoic, the

Haiyuan–Liupanshan fault zone has been dominated by sinistral strike-slip movement because the deep part of the Liupanshan fault zone was limited by the stable and rigid crystallization base of the Ordos massif (e.g., Wang W. et al., 2013), which has further preserved the evolution of the Zhenghua structure, creating the current geomorphological and structural features, such as Liupanshan and Xiaoguanshan (Figure 9C).

In summary, based on previous geochemical results of rocks and our P-wave receiver function results, we believe that the tectonic evolutionary process of the Linxia block, Longzhong block, and southwestern margin of the Ordos block in the study area was as follows:

1) In the late Palaeozoic–late Cambrian, between the Qaidam–Qilian block and the North China plate, the Qilian Ocean was still an ocean basin, the Qaidam–Qilian block was an active continental margin, and the North China block was a passive continental margin. After the Early Ordovician, the Qilian Ocean began to subduct westwards, the Japanese-style island arc initially formed, and the middle and lower crusts in the eastern margin of the Qaidam–Qilian block began to undergo structural shortening and structural uplift under the stress of passive compression. At the same time, the oceanic lithosphere began to subduct under the Qilian Ocean block, forming a Mariana-style island arc, and the Longzhong block first appeared (Figure 9A). 2) In the Late Ordovician-early Silurian, with the closure of the Qilian Ocean, the oceanic crust continued to subduct, and the Mariana-style island arc and Japanese-style island arc collided. The collisional position of the two island arcs may be the initial position of the Maxianshan fault, accompanied by the subduction of the oceanic crust, and ferromafic mélanges were produced near the Maxianshan fault zone under compressive stress. From the late Palaeozoic to Mesozoic, the eastern part of the Qilian Ocean entered the stage of arc–continent collisional deformation, and the Maxianshan fault and Liupanshan fault zone in the study area developed Triassic magmatic rocks, indicating that the combined postcollisional block zone provided a channel for magma emplacement. During the Middle Jurassic–Early Cretaceous, the Linxia block and the Longzhong block experienced differential and rapid uplift, with horizontal and lateral shortening of 15% (Darby and Ritts, 2002). The tectonic uplift events of this period are recorded in the entire Qilian Mountain orogenic belt (Figure 9B). 3) Since the Cenozoic (~15–7 Ma), the tectonic evolution of the study area has been affected by the long-distance effect of the continental collision between the Indian plate and the Eurasian plate, and the tectonic activities are mainly carried out along active faults, such as the Yuan–Liupanshan fault, the Maxianshan fault, and the Northwest Qinling fault. Due to the limitation of the North China plate and the limited deformation space, the late Mesozoic boundary faults were reactivated and controlled by the positive flower structure, the Haiyuan–Liupanshan fault zone was partially uplifted, and the Liupanshan structural belt was initially formed. As the northeast edge of the plateau continued to grow and expand to the periphery, the Haiyuan–Liupanshan fault zone was dominated by sinistral strike-slip movement, which promoted the development of the positive flower structure in the eastern margin of the Longzhong block and shaped the current geomorphic features of Madongshan and Liupanshan (Figure 9C).

Conclusion

In summary, through the analysis of the PRFs, crustal thickness, Poisson's ratio, and CCP results of 33 mobile stations in the eastern section of the Qilian orogenic belt on the northeastern margin of the Qinghai–Tibet Plateau, and based on the results of rock geochemistry, magnetotellurics, and seismic reflection sections in the study area, the following preliminary conclusions have been obtained:

1) The Maxianshan fault is an important boundary fault that divides the Linxia block and the Longzhong block. The crustal layered structure of the Linxia block is obvious, and there is a low-velocity anomaly in the middle and lower crust, which may contain saline fluid and has the characteristics of a Japanese-type island arc. 2) The layered structure of the upper crust of the Longzhong block is significant, while the layered structure of the middle and lower crust is weak and presents weak low-velocity characteristics, showing the characteristics of oceanic-island basaltic crust. The Longzhong block may have originally been formed by Mariana-type island arcs. 3) The Conrad interface and the Moho lateral variation in the southwestern margin of the Ordos block are weak, showing the characteristics of a stable craton. 4) Our calculation results show that the Maxianshan fault cuts through the Earth's crust and is a continuous west-dipping negative seismic phase in the CCP section. The fault zone is the suture line between the Linxia block and the Longzhong block. 5) The middle and upper crust of the Liupanshan tectonic belt is thrust upwards on the southwestern margin of the Ordos block. We believe that this is deep structural evidence of the Cenozoic uplift of the Liupanshan structural belt. 6) We have established the tectonic evolutionary process of early Palaeozoic microcontinental splicing, late Mesozoic lithospheric crustal shortening, and Cenozoic plateau lateral growth and expansion in the study area.

Data availability statement

The original contributions presented in the study are included in the article/Supplementary Material, further inquiries can be directed to the corresponding authors.

Author contributions

YZC: data curation, methodology, investigation, formal analysis, writing- original draft preparation, visualization. RG: conceptualization, methodology, investigation, writing-review, editing, supervision, project administration, funding acquisition. JC: data curation, methodology. ZL and WL: supervision, project administration, visualization. GW, HC, RH, XN, and GW: data curation, software. SC and YGC: software, formal analysis, investigation. All authors contributed to the article and approved the submitted version.

Funding

Conflict of interest

The authors declare that the research was conducted in the absence of any commercial or financial relationships that could be construed as a potential conflict of interest.

Publisher's note

All claims expressed in this article are solely those of the authors and do not necessarily represent those of their affiliated organizations, or those of the publisher, the editors and the reviewers. Any product that may be evaluated in this article, or claim that may be made by its manufacturer, is not guaranteed or endorsed by the publisher.

Supplementary material

The Supplementary Material for this article can be found online at: https://www.frontiersin.org/articles/10.3389/feart.2023.1193167/full#supplementary-material

References

Ammon, C, J., Randall, G., E., and Zandt, G. (1990). On the Nonuniqueness of Receiver function inversions. *J. Geophys. Res. Solid Earth* 95, 15303–15318. doi:10.1029/JB095iB10p15303

Andrew, V. Z., Chen, W., Wang, Z. Z., Levy, D. A., Li, B., Xiong, X., et al. (2019). Underthrusting and duplexing beneath the northern Tibetan Plateau and the evolution of the Himalayan-Tibetan orogen. *Lithosphere* 11 (2), 209–231. doi:10.1130/l1042.1

Burchfiel, B, C., Deng, Q, D., Peter, M., Royden, L., Yipeng, W., Peizhen, Z., et al. (1989). Intracrustal detachment within zones of continental deformation. *Geology* 17 (8), 748–752. doi:10.1130/0091-7613(1989)017<0448:idwzoc>2.3.co;2

Chen, J, H., Liu, Q, Y., Li, S, C., Guo, B., and Lai, Y. G. (2005). Crust and upper mantle S-wave velocity structure across Northeastern Tibetan Plateau and Ordos block. *Chin. J. Geophys.* 48 (2), 369–379. doi:10.1002/cjg2.663

Chen, L., Wang, X., Wang, X., Wei, Z. G., and Zhang, J. Y. (2022). Advances and perspectives for receiver function imaging of the Earth's internal discontinuities and velocity structures. *Rev. Geophys. Planet. Phys.* 53 (6), 680–701. doi:10.19975/j.dqyxx.2022-029

Chen, Y. F., Chen, J. H., Guo, B., Li, S. C., Qi, S. H., Zhao, P. P., et al. (2020). Crustal structure and deformation between different blocks in the northern part of the Western margin of Ordos. *Chin. J. Geophys.* 63 (3), 886–896. doi:10.6038/cjg2020N0211

Chen, Y, L., Niu, F, L., Liu, R, F., Huang, Z., Tkalčić, H., Sun, L., et al. (2010). Crustal structure beneath China from receiver function analysis. *J. Geophys. Research:Solid Earth* 115, B03307. doi:10.1029/2009JB006386

Cheng, F., Jolivet, M., Guo, Z., Lu, H., Zhang, B., Li, X., et al. (2020). Jurassic–early Cenozoic tectonic inversion in the Qilian Shan and Qaidam Basin, north Tibet: New insight from seismic reflection, isopach mapping, and drill core data. *J. Geophys. Res. Solid Earth* 124, 12077–12098. doi:10.1029/2019JB018086

Cheng, H., Lu, T. Y., and Cao, D. D. (2016). Coupled Lu-Hf and Sm-Nd geochronology constrains blueschist-facies metamorphism and closure timing of the Qilian Ocean in the North Qilian orogen. *Gondwana Res.* 34, 99–108. doi:10.1016/j.gr.2016.03.008

Cheng, S. Y., Zhang, G. W., and Li, L. (2003). Lithospheric electrical structure of the Qinling orogen and its geodynamic implication. *Chin. J. Geophys.* 46 (3), 390–397. doi:10.1002/cjg2.3373

Cheng, Y., Z., Gao, R., Lu, Z., W., Li, W., Su, H., Han, R., et al. (2022). Meso-cenozoic tectonic evolution of the Kexueshan basin, northwestern Ordos, China: Evidence from palaeo-tectonic stress fields Analyses. *Front. Earth Sci.* 10, 845475. doi:10.3389/feart. 2022.845475

Cheng, Y. Z., Shi, W., Zhao, G. C., Wang, T. Y., Yang, Q., Qin, X., et al. (2019). Superimposed deformation in the Kexueshan area, the Western periphery of the Ordos block. *J. Earth Sci. Environ.* (2), 16. (in Chinese).

Christensen, N, I. (1996). Poisson's ratio and crustal seismology. *J. Geophys Res.* 101, 3139–3156. doi:10.1029/95JB03446

Clark, M, K., and Royden, L. H. (2000). Topographic ooze: Building the easternmargin of Tibet by lower crustal flow. *Geology* 28 (2), 703–706. doi:10.1130/ 0091-7613(2000)028<0703:tobtem>2.3.co;2

Cui, Z. Z., Li, Q. S., Wu, C. D., Yin, Z. X., and Liu, H. B. (1995). The crustal and deep structures in Golmud-Ejin Qi GGT. *Chin. J. Geophys.* 38 (S2), 15–28.

Darby, B. J., and Ritts, B. D. (2002). Mesozoic contractional deformation in the middle of the Asian tectonic collage: The intraplate western Ordos fold–thrust belt, China. *Earth Planet Sci. Lett.* 205, 13–24. doi:10.1016/S0012-821X(02) 01026-9

Ding, L., Kapp, P., Cai, F., Garzione, C. N., Xiong, Z., Wang, H., et al. (2022). Timing and mechanisms of Tibetan Plateau uplift. *Nat. Rev. Earth Environ.* 3 (10), 652–667. doi:10.1038/s43017-022-00318-4

Ding, Z., Cheng, B., Dong, Y., and Zhao, D. (2017). Seismic imaging of the crust and uppermost mantle beneath the Qilian Orogenic Belt and its geodynamic implications. *Tectonophysics* 705, 63–79. doi:10.1016/j.tecto.2017.03.016

Dong, S., Zhang, Y., Li, H., Shi, W., Xue, H., Li, J., et al. (2018). The Yanshan orogeny and late mesozoic multi-plate convergence in East Asia Commemorating 90th years of the "Yanshan orogeny. *Sci. China Earth Sci.* 61, 1888–1909. doi:10.1007/s11430-017- 9297-y

Dong, Y., and Santosh, M. (2016). Tectonic architecture and multiple orogeny of the Qinling orogenic belt, Central China. *Gondwana Res.* 29, 1–40. doi:10.1016/j.gr.2015. 06.009

Dueker, K, G., and Sheehan, A, F. (1997). Mantle discontinuity structure from midpoint stacks of converted P to S waves across the Yellowstone hotspot track. *J. Geophys. Res. Solid Earth* 102, 8313–8327. doi:10.1029/96JB03857

Duvall, A. R., Clark, M. K., Kirby, E., Farley, K. A., Craddock, W. H., Li, C., et al. (2013). Low-temperature thermochronometry along the Kunlun and Haiyuan faults, NE Tibetan plateau: Evidence for kinematic change during late-stage orogenesis. *Tectonics* 32, 1190–1211. doi:10.1002/tect.20072

Galvé, A., Hirn, A., Jiang, M., Gallart, J., de Voogd, B., Lépine, J. C., et al. (2002). Modes of raising northeastern Tibet probed by explosion seismology. *Earth Planet. Sci. Lett.* 203 (1), 35–43. doi:10.1016/S0012-821X(02)00863-4

Gan, W, J., Zhang, P, Z., Shen, Z, K., Niu, Z., Wang, M., Wan, Y., et al. (2007). Present-day crustal motion within the Tibetan Plateau inferred from GPS measurements. *J. Geophys. Res. Solid Earth* 112, B08416. doi:10.1029/2005JB004120

Gao, R., Ma, Y. S., Li, Q. S., Zhu, X., Zhang, J. S., Wang, H. Y., et al. (2006). Structure of the lower crust beneath the Songpan block and West Qinling orogen and their relation as revealed by deep seismic reflection profiling. *Geol. Bull. China* 25 (12), 1361–1367. doi:10.3969/j.issn.1671-2552.2006.12.003

Gao, R., Wang, H. Y., Wang, C. S., Yin, A., Zhang, Y. X., Li, Q. S., et al. (2011). Lithospheric deformation shortening of the northeastern Tibetan plateau: Evidence from Reprocessing of deep seismic reflection data. *Acta Geosci. Sin.* 29 (2), 14–27. doi:10.3975/cagsb.2011.05.01

Gao, R., Wang, H., Yin, A., Dong, S., Kuang, Z., Zuza, A. V., et al. (2013). Tectonic development of the northeastern Tibetan Plateau as constrained by high-resolution deep seismic-reflection data. *Lithosphere* 5 (6), 555–574. doi:10.1130/L293.1

Gao, R., Zhou, H., Lu, Z. W., Guo, X. Y., Li, W. H., Wang, H. Y., et al. (2022). Deep seismic reflection profile reveals the deep process of continent-continent collision on the Tibetan Plateau. *Earth Sci. Front.* 29 (2), 14–27. doi:10.13745/j.esf.sf.2021.8.10

Gaudemer, Y., Tapponnier, P., Meyer, B., Peltzer, G., Shunmin, G., Zhitai, C., et al. (1995). Partitioning of crustal slip between linked, active faults in the eastern Qilian Shan, and evidence for a major seismic gap, the 'Tianzhu gap', on the Western Haiyuan Fault, Gansu (China). *Geophys. J. Int.* 120 (3), 599–645. doi:10.1111/j.1365-246X.1995. tb01842.x

Gehrels, G. E., Yin, A., and Wang, X. F. (2003). Detrital-zircon geochronology of the northeastern Tibetan plateau. *Geol. Soc. amer.Bul.* 115 (7), 881–896. doi:10.1130/0016- 7606(2003)115<0881:DGOTNT>2.0.CO;2

Gong, M., Li, X. F., Zhang, S. X., Luo, Y., Zeng, X. F., and Liu, L. (2015). Crustal thickness and Poisson's ratio of Hebei and adjacent areas from teleseismic receiver functions. *Earthquake* 35 (2), 34–42. (in Chinese).

Guo, P., Liu, C., Wang, J., and Deng, Y. (2018a). Detrital zircon geochronology of the Jurassic strata in the Western Ordos Basin, north China: Constraints on the provenance and its tectonic implication. *Geol. J.* 53, 1482–1499. doi:10.1002/gj.2968

Guo, P., Liu, C., Wang, J., Deng, Y., Mao, G., and Wang, W. (2018b). Detrital-zircon geochronology of the Jurassic coal-bearing strata in the Western Ordos Basin, north

China: Evidences for multi-cycle sedimentation. *Front* 9, 1725–1743. doi:10.1016/j.gsf. 2017.11.003

Guo, X, Y., Gao, R., Li, S, Z., Xu, X., Huang, X., Wang, H., et al. (2016). Lithospheric architecture and deformation of NE Tibet: New insights on the interplay of regional tectonic processes. *Earth Planet. Sci. Lett.* 449, 89–95. doi:10.1016/j.epsl.2016.05.045

Guo, X, Y., Gao, R., Wang, H, Y., Li, W., Keller, G. R., Xu, X., et al. (2015). Crustal architecture beneath the Tibet-Ordos transition zone, NE Tibet, and the implications for plateau expansion. *Geophys. Res. Lett.* 42 (24), 10631–10639. doi:10.1002/ 2015GL066668

Han, S., Han, J. T., Liu, G. X., Wang, H. Y., and Liang, H. D. (2016). Crust and upper mantle electrical structure and tectonic deformation of the northeastern margin of the Tibetan Plateau and the adjacent Ordos Block. *Chin. J. Geophys.* 59 (11), 4126–4138. doi:10.6038/cjg20161116

Hao, S., Huang, Z., Han, C., Wang, L., Xu, M., Mi, N., et al. (2021). Layered crustal azimuthal anisotropy beneath the northeastern Tibetan Plateau revealed by Rayleigh-wave Eikonal tomography. *Earth Planet. Sci. Lett.* 563, 116891. doi:10.1016/j.epsl.2021. 116891

Hart, S. R., Glassley, W. E., and Karig, D. E. (1972). Basalts and sea floor spreading behind the Mariana island arc. *Earth Planet. Sci. Lett.* 15 (1), 12–18. doi:10.1016/0012- 821X(72)90023-4

He, S. P., Wang, H. L., Chen, J. L., Xu, X., Zhang, H., Ren, G., et al. (2008). LA-ICPMS U-Pb zircon geochronology of basic dikes within Maxianshan rock group in the central Qilian mountains and its tectonic implications. *Earth Sci.-J. China Univ. Geosci.* 33 (1), 35–45. doi:10.1016/S1002-0705(07)60015-6

Ji, S. C., Wang, Q., and Yang, W. C. (2009). Correlation between crustal thickness and Poisson's ratio in the North China craton and its implication for lithospheric Thinning. *Acta Geol. Sin.* 83 (3), 324–330. (in Chinese).

Jia, S. X., Zhang, X, K., Zhao, J, R., Wang, F., Zhang, C., Xu, Z., et al. (2009). Deep seismic sounding data reveal the crustal structures beneath Zoige basin and its surrounding folded orogenic belts. *Sci. China Ser. D-Earth Sci.* 53, 203–212. doi:10. 1007/s11430-009-0166-0

Jin, S., Zhang, L. T., Jin, Y. J., Wei, W. B., Ye, G. F., et al. (2012). Crustal electrical structure along the Hezuo-Dajing profile across the northeastern margin of the Tibetan plateau. *Chin. J. Geophys.* 55 (12), 3979–3990. doi:10.6038/j.issn.0001-5733.2012.12.010

Kapp, P., DeCelles, P. G., Gehrels, G. E., Heizler, M., and Ding, L. (2007). Geological records of the Lhasa-Qiangtang and Indo-Asian collisions in the Nima area of central Tibet. *Geol. Soc. Am. Bull.* 119, 917–933. doi:10.1130/B26033.1

Karplus, M. S., Zhao, W., Klemperer, S. L., Wu, Z., Mechie, J., Shi, D., et al. (2011). Injection of Tibetan crust beneath the south Qaidam Basin: Evidence from INDEPTH IV wide-angle seismic data. *J. Geophys. Res.* 116, B07301. doi:10. 1029/2010JB007911

Kennett, B, L., and Engdahl, E, R. (1991). Traveltimes for global earthquake location and phase identification. *Geophys. J. Int.* 105 (2), 429–465. doi:10.1111/j.1365-246X. 1991.tb06724.x

Langston, C, A. (1979). Structure under Mount Rainier, Washington, inferred from teleseismic body waves. *J. Geophys. Res.* 84 (B9), 4749–4762. doi:10.1029/ JB084iB09p04749

Li, Q, S., Peng, S, P., and Gao, R. (2004). Deep tectonic background of the great east Kunlun earthquake. *Chin. J. Geophys.* 25 (1), 11–16. (in Chinese).

Li, S, L., and Lai, X, L. (2006). Preliminary study on quasi tri-junction in northeastern margin of Qinghai-Tibet Plateau. *J. Geodesy Geodyn.* 26, 10–14. (in Chinese).

Li, W. H., Gao, R., Wang, H. Y., Li, Y. K., Li, H. Q., Hou, H. S., et al. (2017). Crustal structure beneath the Liupanshan fault zone and adjacent regions. *Chin. J. Geophys.* 60 (6), 2265–2278. (in Chinese). doi:10.6038/cjg20170619

Li, Y. H., Wu, Q. J., An, Z. H., Tian, X. B., Zeng, R. S., Zhan, R. Q., et al. (2006). The Poisson ratio and crustal structure across the NE Tibetan Plateau determined from receiver functions. *Chin. J. Geophys.* 49 (5), 1359–1368. (in Chinese).

Ligorria, J, P., and Ammon, C, J. (1999). Iterative deconvolution and receiver function estimation. *Bull. Seismol. Soc. Am.* 89 (5), 1395–1400. doi:10.1785/ BSSA0890051395

Lin, X. B., Chen, H, L., Wyrwoll, K, H., and Cheng, X, G. (2010). Commencing uplift of the Liupan Shan since 9.5 Ma: Evidences from the Sikouzi section at its east side. *J. Asian Earth Sci.* 37, 350–360. doi:10.1016/j.jseaes.2009.09.005

Lin, X., Chen, H., Wyrwoll, K.-H., Batt, G. E., Liao, L., and Xiao, J. (2011). The uplift history of the Haiyuan-Liupan Shan region northeast of the present Tibetan plateau: Integrated constraint from stratigraphy and thermochronology. *J. Geol.* 119, 372–393. doi:10.1086/660190

Liu, C., Zhao, H., Wang, F., and Chen, H. (2005). Attributes of the mesozoic structure on the west margin of the Ordos Basin. *Acta Geol. Sin.* 79, 737–739. doi:10.1360/ gs050303

Liu, C., Zhao, H., Zhao, J., Wang, J., Zhang, D., and Yang, M. (2008a). Temporo-spatial Coordinates of evolution of the Ordos Basin and its mineralization responses. *Acta Geol. Sin.* 82, 1229–1243. doi:10.1111/j.1755-6724.2008.tb00725.x

Liu, M, J., Li, S., L., Fang, S., M., Fan, J. C., and Zhao, L. (2008b). Study on crustal composition and geodynamics using seismic velocities in the northeastern margin of the Tibetan Plateau. *Chin. J. Geophys.* 51 (2), 275–297. (in Chinese). doi:10.1002/cjg2.1219

Liu, M, J., Mooney, W, D., Li, S., L., Okaya, N., and Detweiler, S. (2006). Crustal structure of the northeastern margin of the Tibetan plateau from the Songpan-Ganzi terrane to the Ordos Basin. *Tectonophysics* 420 (1-2), 253–266. doi:10.1016/j.tecto.2006.01.025

Liu, Q, Y., Rainer, K., and Li, S. C. (1996). Maximal Likelihood estimation and nonlinear inversion of the complex receiver function Spectrum ratio. *Chin. J. Geophys.* 39 (04), 500–511. (in Chinese). doi:10.1007/BF02029074

Owens, T, J., and Zandt, G. (1997). Implications of crustal property variations for models of Tibetan plateau evolution. *Nature* 387, 37–43. doi:10.1038/387037a0

Pei, X. Z., Liu, H. B., Ding, S. P., Li, Z. C., Hu, B., Sun, R. Q., et al. (2006). Geochemical characteristics and tectonic significance of the Meta volcanic rocks in the Liziyuan group from Tianshui area, western Qinling orogen. *Geotect. Metallogenia* 30 (02), 193–205. doi:10.3969/j.issn.1001-1552.2006.02.010

Peng, H., Wang, J., Liu, C., Ma, M., Ma, Q., Li, K., et al. (2022c). Meso-Cenozoic growth of the eastern Qilian Shan, northeastern Tibetan Plateau margin: Insight from borehole apatite fission-track thermochronology in the Xiji Basin. *Mar. Petroleum Geol.* 143, 105798. doi:10.1016/j.marpetgeo.2022.105798

Peng, H., Liu, X., Liu, C., Hui, X., Quan, X., Zhang, T., et al. (2022a). Spatialtemporal evolution and the dynamic background of the translation of Mid-Late Mesozoic tectonic regimes of the southwest Ordos Basin margin. *Acta Geol. Sin.* 96, 387–402. doi:10.19762/j.cnki.dizhixuebao.2021077

Peng, H., Wang, J., Liu, C., Huang, L., Zattin, M., Li, K., et al. (2022b). Meso-Cenozoic growth of the eastern Qilian Shan, northeastern Tibetan Plateau margin: Insight from borehole apatite fission-track thermochronology in the Xiji Basin. *Tectonophysics* 823, 105798. doi:10.1016/j.marpetgeo.2022.105798

Peng, H., Wang, J., Liu, C., Zhang, S., Zattin, M., Wu, N., et al. (2019). Thermochronological constraints on the meso-Cenozoic tectonic evolution of the Haiyuan-Liupanshan region, northeastern Tibetan plateau. *J. Asian Earth Sci.* 183, 103966. doi:10.1016/j.jseaes.2019.103966

Peng, H., Wang, J., Zattin, M., Liu, C. Y., Han, P., and Zhang, S. H. (2018). Late Triassic-early Jurassic uplifting in eastern Qilian Mountain and its geological significance: Evidence from apatite fission track thermochronology. *Earth Sci.* 43, 1983–1996. doi:10.3799/dqkx.2018.608

Ren, Z., Xiao, H., Liu, L., Zhang, S., Qin, Y., and Wei, C. (2005). The evidence of fission-track data for the study of tectonic thermal history in Qinshui Basin. *Chin. Sci. Bull.* 50, 104–110. doi:10.1007/BF03184091

Ren, Z., Yu, Q., Cui, J., Qi, K., Chen, Z., Cao, Z., et al. (2017). Thermal history and its controls on the oil and gas of the Ordos Basin. *Earth Sci. Front.* 24, 137–148. doi:10.13745/j.esf.2017.03.012

Shi, L., Li, Y., Wang, W., and Ma, Y. (2022). Crustal structure beneath the northeastern margin of the Tibetan Plateau constrained by receiver functions and gravity data. *Tectonophysics* 841, 229584. doi:10.1016/j.tecto.2022.229584

Song, S. G., Niu, Y. L., Su, L., and Xia, X. H. (2013). Tectonics of the North Qilian orogen. NW China. *Gondwana Res.* 23 (4), 1378–1401. doi:10.1016/j.gr.2012.02.004

Song, S. G., Zhang, L. F., Niu, Y. L., Su, L., Song, B., and Liu, D. (2006). Evolution from oceanic subduction to continental collision: A case study from the northern Tibetan plateau based on geochemical and geochronological data. *J. Petrol.* 47 (3), 435–455. doi:10.1093/petrology/egi080

Tang, X., Guo, Z., and Chen, H. (1992). *The study and Petroleum Prospect of thrust nappe in the West margin of Shaanxi-Gansu-Ningxia basin.* Xi'an: Northwest University Press. (in Chinese).

Tapponnier, P., Xu, Z, Q., Roger, F., Meyer, B., Arnaud, N., Wittlinger, G., et al. (2001). Oblique stepwise rise and growth of the Tibet Plateau. *Science* 294, 1671–1677. doi:10.1126/science.105978

Taylor, M., and Yin, A. (2009). Active structures of the Himalayan-Tibetan orogen and their relationships to earthquake distribution, contemporary strain field, and Cenozoic volcanism. *Geosphere* 5 (3), 199–214. doi:10.1130/Ges00217.1

Teng, J, W. (1974). Deep reflected waves and the structure of the Earth crust of the eastern part of Chaidam basin. *Chin. J. Geophys.* 17 (02), 122–135. (in Chinese).

Teng, J, W., Zhang, Z, J., Zhang, X, K., Wang, C., Gao, R., Yang, B., et al. (2013). Investigation of the Moho discontinuity beneath the Chinese mainland using deep seismic sounding profiles. *Tectonophysics* 609, 202–216. doi:10.1016/j.tecto.2012.11.024

Tian, Q, J., and Ding, G, Y. (1998). The tectonic feature of a quasi-trijunction in the northeastern corner of Qinghai-Xizang Plateau. *Earthq. Res. China* 14 (4), 17–35. (in Chinese).

Tian, X, B., Bai, Z, N., Klemperer, S, L., Liang, X., Liu, Z., Wang, X., et al. (2021). Crustal-scale wedge tectonics at the narrow boundary between the Tibetan Plateau

and Ordos block. *Earth Planet. Sci. Lett.* 554, 116700. doi:10.1016/j.epsl.2020.116700

Tian, X, B., Wu, Q, J., Zhang, Z, J., Teng, J., and Zeng, R. (2005). Joint imaging by teleseismic converted and multiple waves and its application in the INDEPTH-III passive seismic array. *Geophys. Res. Lett.* 32 (10), L21315–L22005. doi:10.1029/2005GL023686

Tian, X, B., and Zhang, Z, J. (2013). Bulk crustal properties in NE Tibet and their implications for deformation model. *Gondwana Res.* 24 (2), 548–559. doi:10.1016/j.gr.2012.12.024

Tong, W, W., Wang, L, S., Mi, N., Xu, M, J., Li, H., Yu, D, Y., et al. (2007). Using receiver function to study the structure characteristics of crust and upper mantle in Liupanshan area. *Sci. China Ser. D-Earth Sci.* 37, 193–198. doi:10.1360/zd2007-V37-IS1-P193-198

Vergne, J., Wittlinger, G., Hui, Q., Tapponnier, P., Poupinet, G., Mei, J., et al. (2002). Seismic evidence for stepwise thickening of the crust across the NE Tibetan plateau. *Earth Planet. Sci. Lett.* 203 (1), 25–33. doi:10.1016/S0012-821X(02)00853-1

Wang, E., Kirby, E., Furlong, K. P., van Soest, M., Xu, G., Shi, X., et al. (2012). Two-phase growth of high topography in eastern Tibet during the Cenozoic. *Nat. Geosci.* 5, 640–645. doi:10.1038/ngeo1538

Wang, G., Li, S., Li, X., Zhao, W., Zhao, S., Suo, Y., et al. (2019). Destruction effect on Meso-Neoproterozoic oil-gas traps derived from Meso-Cenozoic deformation in the North China Craton. *Precambrian Res.* 333, 105427. doi:10.1016/j.precamres.2019.105427

Wang, J. Q. (2007). Reconstruction of the Early Crataceous Basin and its evolution in southwest Ordos. Master dissertation of Northwest University, 1–84.

Wang, Q., Gao, Y., Shi, Y. T., and Wu, J. (2013). Seismic anisotropy in the uppermost mantle beneath the northeastern margin of Qinghai-Tibet plateau: Evidence from shear wave splitting of SKS, PKS and SKKS. *Chin. J. Geophys.* 56 (3), 892–905. (in Chinese). doi:10.6038/cjg20130318

Wang, W., Kirby, E., Zhang, P., Zheng, D., Zhang, G., Zhang, H., et al. (2013). Tertiary basin evolution along the northeastern margin of the Tibetan plateau: Evidence for basin formation during Oligocene transtension. *Geol. Soc. Am. Bull.* 125, 377–400. doi:10.1130/B30611.1

Wang, W., Zhang, P., Zheng, D., Pang, J., Yang, J. M., Yin, S. J., et al. (2014). A folding study of Antarctic krill (Euphausia superba) alkaline phosphatase using denaturants. *Earth Sci. Front.* 21, 266–274. doi:10.1016/j.ijbiomac.2014.07.001

Wang, X., Li, Y., Ding, Z., Zhu, L., Wang, C., Bao, X., et al. (2017). Three-dimensional lithospheric S wave velocity model of the NE Tibetan Plateau and Western North China Craton. *J. Geophys. Res. Solid Earth* 122 (8), 6703–6720. doi:10.1002/2017JB014203

Wei, Y., Tian, X., Duan, Y., and Ding, Z. (2022). The lithospheric structure beneath the northeastern Tibetan Plateau and Western North China Craton from S receiver function imaging and its implications for lateral growth of the plateau. *Tectonophysics* 838, 229466. doi:10.1016/j.tecto.2022.229466

Wu, H. Q., Feng, Y. M., and Song, S. G. (1993). Metamorphism and deformation of blueschist belts and their tectonic implications, North Qilian Mountains, China. *J. Metamorph. Geol.* 11 (4), 523–536. doi:10.1111/j.1525-1314.1993.tb00169.x

Wu, J., Liu, Y., Zhong, S., Wang, W., Cai, Y., Wang, W., et al. (2022). Lithospheric structure beneath Ordos Block and surrounding areas from joint inversion of receiver function and surface wave dispersion. *Sci. China Earth Sci.* 65 (7), 1399–1413. doi:10.1007/s11430-021-9895-0

Xia, S. B., Wang, X. B., Min, G., Hu, Y. B., Li, D. W., Kong, F. T., et al. (2019). Crust and uppermost mantle electrical structure beneath Qilianshan Orogenic Belt and Alxa block in northeastern margin of the Tibetan Plateau. *Chin. J. Geophys.* 62 (03), 950–966. doi:10.6038/cjg2019M0552

Xiao, W. J., Windley, B. F., Yong, Y., Yan, Z., Yuan, C., Liu, C., et al. (2009). Early Paleozoic to Devonian multiple-accretionary model for the Qilian Shan, NW China. *J. Asian Earth Sci.* 35, 323–333. doi:10.1016/j.jseaes.2008.10.001

Xin, Z, H., Han, J, T., Gao, R., Guo, X., Liang, H., Kang, J., et al. (2021). Electrical structure of the eastern segment of the Qilian orogenic belt revealed by 3-D inversion of magnetotelluric data: New insights into the evolution of the northeastern margin of the Qinghai-Tibet Plateau. *J. Asian Earth Sci.* 210, 104707. doi:10.1016/j.jseaes.2021.104707

Xu, Q., and Zhao, J, M. (2008). A review of the receiver function method. *Prog. Geophys.* 23 (6), 1709–1716. (in Chinese).

Xu, X., Niu, F., Ding, Z., and Chen, Q. (2018). Complicated crustal deformation beneath the NE margin of the Tibetan plateau and its adjacent areas revealed by multi-station receiver-function gathering. *Earth Planet. Sci. Lett.* 497, 204–216. doi:10.1016/j.epsl.2018.06.010

Xu, Z, Q., Xu, H, F., Zhang, J, X., Li, H, B., Zhu, Z, Z., Qu, J, C., et al. (1994). Proliferating terrane and its dynamics of the Caledonian subduction complex in the Nanshan mountains. North Qilian Corridor. *Acta Geol. Sin.* 1, 1–15. doi:10.1111/j.1755-6724.1994.mp7003001.x

Yang, J, S., Xu, Z, Q., Zhang, J, X., Shuguang, S., Cailai, W., Rendeng, S., et al. (2002). Early Palaeozoic North Qaidam UHP metamorphic belt on the north-eastern Tibetan

plateau and a paired subduction model. *Terra nova.* 14 (5), 397–404. doi:10.1046/j.1365-3121.2002.00438.x

Yin, A. (2010a). Cenozoic tectonic evolution of Asia: A preliminary synthesis. *Tect.* 488, 293–325. doi:10.1016/j.tecto.2009.06.002

Yin, A., and Harrison, T, M. (2000). Geologic evolution of the Himalayan-Tibetan orogen. *Annu. Rev. Earth Planet Sci.* 28, 211–280. doi:10.1146/annurev. earth.28.1.211

Yin, H, F., and Zhang, K, X. (1998). The evolution and characteristics of the central orogenic belt. *Earth Sci.* 23, 438–441. (in Chinese). doi:10.3321/j.issn:1000-2383.1998. 05.001

Yu, C, Q., Zheng, Y, C., and Shang, X, F. (2017). Crazyseismic: A MATLAB GUI-based software package for passive seismic data preprocessing. *Seismol. Res. Lett.* 88 (2A), 410–415. doi:10.1785/0220160207

Zeng, R, S., Ding, Z, F., and Wu, Q, J. (1994). A review on the lithospheric structures in the Tibetan Plateau and constraints for dynamics. *Chin. J. Geophys.* 37 (S2), 425–443. (in Chinese). doi:10.1007/BF00879582

Zhan, Y., Yang, H., Zhao, G. Z., Zhao, L. Q., and Sun, X. Y. (2017). Deep electrical structure of crust beneath the Madongshan step area at the Haiyuan fault in the northeastern margin of the Tibetan plateau and tectonic implications. *Chin. J. Geophys.* 60 (6), 2371–2384. (in Chinese). doi:10.6038/cjg20170627

Zhang, G. W., Cheng, S. Y., Guo, A. L., Dong, Y. P., Lai, S. C., and Yao, A. P. (2004). Mianlue paleo-suture on the southern margin of the Central Orogenic System in Qinling-Dabie with a discussion of the assembly of the main part of the continent of China. *Geol. Bull. China* 23 (9), 846–853. doi:10.3969/j.issn.1671-2552.2004.09.005

Zhang, H. S., Gao, R., Tian, X. B., Teng, J. W., Li, Q. S., Ye, Z., et al. (2015). Crustal Swave velocity beneath the northeastern Tibetan plateau inferred from teleseismic Pwave receiver functions. *Chin. J. Geophys.* 58 (11), 3982–3992. (in Chinese). doi:10.6038/cjg20151108

Zhang, H. S., Li, Q. S., Gao, R., Ye, Z., and Gong, C. (2016). The lithospheric structure beneath the northeastern Tibetan Plateau inferred from S-wave receiver functions. *Chin. J. Geol.* 51 (1), 5–14. doi:10.3969/j.issn.0563-5020.2016.01.002

Zhang, P, Z., Shen, Z, K., Wang, M., Gan, W., Bürgmann, R., Molnar, P., et al. (2004). Continuous deformation of the Tibetan Plateau from global positioning system data. *Geology* 32, 809–812. doi:10.1130/G20554.1

Zhang, Z, J., Bai, Z, M., Klemperer, S, L., Tian, X., Xu, T., Chen, Y., et al. (2013). Crustal structure across northeastern Tibet from wide-angle seismic profiling: Constraints on the Caledonian Qilian orogeny and its reactivation. *Tectonophysics* 606, 140–159. doi:10.1016/j.tecto.2013.02.040

Zhang, Z, J., Klemperer, S., Bai, Z, M., Chen, Y., and Teng, J. (2011). Crustal structure of the Paleozoic Kunlun orogeny from an active-source seismic profile between Moba and Guide in east Tibet, China. *Gond. Res.* 19 (4), 994–1007. doi:10.1016/j.gr.2010.09.008

Zhao, H. G., Liu, C. Y., Yao, Y. M., Wang, F., and Yin, Y. (2007). Differential uplift in the west margin of Ordos Basin since Mesozoic from the fission track evidence. *J. NW Univ.* 37, 470–474. doi:10.1016/S1872-5813(07)60034-6

Zhao, J, F., Liu, C, Y., Huang, L., Zhang, D., Wang, D., and Wang, D. (2019). Paleogeography reconstruction of a multi-stage modified intra-cratonic basin—A case study from the Jurassic Ordos Basin, Western north China craton. *J. Asian Earth Sci.* 190, 104191. doi:10.1016/j.jseaes.2019.104191

Zheng, D., Clark, M. K., Zhang, P., Zheng, W., and Farley, K. A. (2010). Erosion, fault initiation and topographic growth of the North Qilian Shan (northern Tibetan Plateau). *Geosphere* 6, 937–941. doi:10.1130/GES00523.1

Zheng, D., Zhang, P.-Z., Wan, J., Yuan, D., Li, C., Yin, G., et al. (2006). Rapid exhumation at~ 8 Ma on the Liupan Shan thrust fault from apatite fission-track thermochronology: Implications for growth of the northeastern Tibetan plateau margin. *Earth Planet Sci. Lett.* 248, 198–208. doi:10.1016/j.epsl.2006.05.023

Zhong, D, L., and Ding, L. (1996). Rising process of the Qinghai-Xizang (Tibet) Plateau and its mechanism. *Sci. China Ser. D-Earth Sci.* 11, 369–379. doi:10.1360/zd1996-26-4-289

Zhu, D. C., Li, S. M., Cawood, P. A., Wang, Q., Zhao, Z. D., Liu, S. A., et al. (2016). Assembly of the Lhasa and Qiangtang terranes in central Tibet by divergent double subduction. *Lithos* 245, 7–17. doi:10.1016/j.lithos.2015.06.023

Zhu, L, P., and Kanamori, H. (2000). Moho depth variation in southern California from teleseismic receiver functions. *J. Geophys. Res.* 105, 2969–2980. doi:10.1029/1999JB900322